

Dictionary Learning in Fourier Transform Scanning Tunneling Spectroscopy

Sky C. Cheung ^{a,1} John Y. Shin ^{a,1} Yenson Lau,² Zhengyu Chen,² Ju Sun,² Yuqian Zhang,² John N. Wright,^{2,†} and Abhay N. Pasupathy^{1,‡}

¹*Department of Physics, Columbia University, New York, NY 10027 USA*

²*Department of Electrical Engineering,
Columbia University, New York, NY 10027 USA*

(Dated: July 30, 2018)

arXiv:1807.10752v1 [physics.comp-ph] 19 Jul 2018

^a These authors contributed equally to this work

Modern high-resolution microscopes, such as the scanning tunneling microscope, are commonly used to study specimens that have dense and aperiodic spatial structure [1–7]. Extracting meaningful information from images obtained from such microscopes remains a formidable challenge [8–10]. Fourier analysis is commonly used to analyze the underlying structure of fundamental motifs present in an image [2, 4, 6–8, 11]. However, the Fourier transform fundamentally suffers from severe phase noise when applied to aperiodic images [12, 13]. Here, we report the development of a new algorithm based on nonconvex optimization, applicable to any microscopy modality, that directly uncovers the fundamental motifs present in a real-space image. Apart from being quantitatively superior to traditional Fourier analysis, we show that this novel algorithm also uncovers phase sensitive information about the underlying motif structure. We demonstrate its usefulness by studying scanning tunneling microscopy images of a Co-doped iron arsenide superconductor and prove that the application of the algorithm allows for the complete recovery of quasiparticle interference in this material. Our phase sensitive quasiparticle interference imaging results indicate that the pairing symmetry in optimally doped NaFeAs is consistent with a sign-changing s^\pm order parameter.

The past few decades have seen dramatic advances in the understanding of the structure of materials via scattering and microscopy techniques. Scattering techniques are useful when perfect periodicity exists in a material, while microscopy is well-suited for specimens that lack periodicity. Recent advances in microscopy techniques, when coupled with improved computing power, have enabled the scientific community to generate massive, multi-dimensional spatial images of specimens as a function of control parameters such as time, energy, and applied stimulus. Examples of such advanced tools include super-resolution optical microscopy to inspect the structure of proteins beyond the diffraction limit [14], scanning transmission electron microscopy to examine the chemical structure of materials at the atomic scale [15], and scanning tunneling microscopy (STM) to visualize the quantum electronic structure of surfaces with atomic resolution [16]. Fundamentally, a microscope image represents the interaction between the probe and the specimen, and often times sophisticated analysis must

† johnwright@ee.columbia.edu

‡ pasupathy@phys.columbia.edu

be performed to uncover the scientific content present in the image. Specimens of interest for STM studies include metals [1], two-dimensional materials [3], unconventional superconductors [2], topological materials [4, 17], and charge [7] and spin [5, 18] ordered materials, among others. Image analysis of these materials has provided several unique insights into the quantum electronic structure and interactions present within them. Many microscopy techniques utilize the Fourier Transform (FT) [19, 20] for analysis, revealing the characteristic wavelengths present in the image, which are then related to a scientific theory of the specimen being studied. When perfect periodicity exists in an image, the FT provides a concise and accurate description of the image. However, when applied to aperiodic images, the FT suffers from phase noise leading to a fundamental loss of information. With the proliferation of new computing techniques, one may wonder if the maturation of optimization algorithms can be leveraged to extract more information from a microscopy image than through the FT. In this work, we consider a class of images that are of particular importance to microscopy – those that can be perceived as a basic motif, called a kernel, that is repeated aperiodically across the image. Examples of kernels include electronic scattering patterns around atomic defects (in STM) and fluorescence from individual proteins (in optical microscopy). We present the development of an algorithm, based on nonconvex optimization, for analyzing such images that quantitatively extracts the principal motifs present in an image without estimating or averaging over instances of the defect. We demonstrate that this algorithm can elucidate fundamentally new information unavailable through traditional FT analysis. While our methods are generally applicable to a wide range of microscopy techniques, in this work we focus on its application to STM.

STM spectroscopy produces two-dimensional spectroscopic maps of the Local Density of States (LDoS) at position \vec{x} with energy ω , forming a three-dimensional dataset. The contrast in these images stems from local spatial variations of the LDoS, denoted as $\delta\rho(\vec{x}, \omega)$. Measurements in which $\delta\rho(\vec{x}, \omega)$ is ascribed to material defects that cause electron scattering and interference [1] are particularly interesting, and such maps are often called Quasiparticle Interference (QPI) maps. Analysis of QPI maps has uncovered information on the dispersion relations and scattering processes in semimetals [21, 22], high-temperature superconductors [2, 6, 8, 23], and other systems. Let us suppose that the LDoS pattern created by a single defect located at \vec{x} with energy ω is $\delta\rho_0(\vec{x}, \omega)$. This quantity is related to the scattering matrix \hat{T} and bare Green's function \hat{G}_0 through $\delta\rho_0(\vec{x}, \omega) = \frac{-1}{\pi} \text{Im} \left[\langle \vec{x} | \hat{G}_0 \hat{T} \hat{G}_0 | \vec{x} \rangle \right]$

(see Supplementary Information Section I). Accordingly, the STM image from N defects located at $\vec{x}_1, \vec{x}_2, \dots, \vec{x}_N$ is:

$$\delta\rho(\vec{x}, \omega) = \sum_{j=1}^N c_j \delta\rho_0(\vec{x} - \vec{x}_j, \omega) \quad (1)$$

where c_j are constants. A real-world example of such an image is shown in Figure 1(a), obtained on the pnictide superconductor NaFeAs [6].

According to scattering theory, the FT of the QPI image of an individual defect, $\delta\rho_0(\vec{k}, \omega) = \int d\vec{x} e^{-i\vec{k}\cdot\vec{x}} \delta\rho_0(\vec{x}, \omega)$, is correlated with the underlying electronic structure of the material [8–10]. Most materials of interest have sufficient disorder so that the LDoS signatures of different defects overlap. In this situation, it is not possible to identify the isolated defect signature through inspection. Instead, the traditional analysis [7] proceeds by taking the FT of the entire STM image $\delta\rho(\vec{x}, \omega)$ in (1):

$$\delta\rho(\vec{k}, \omega) = \int d\vec{x} e^{-i\vec{k}\cdot\vec{x}} \delta\rho(\vec{x}, \omega) = \delta\rho_0(\vec{k}, \omega) \sum_{j=1}^N c_j \exp\{-i\vec{k}\cdot\vec{x}_j\} \quad (2)$$

While the quantity of interest for QPI analysis is $\delta\rho_0(\vec{k}, \omega)$, the experimental FT image contains a frequency-varying, complex-valued phase factor, $\mathcal{P}(\vec{k}) \equiv \sum_{j=1}^N c_j \exp\{-i\vec{k}\cdot\vec{x}_j\}$. This is illustrated in Figure 1(b), where the Real Part of the FT (Re-FT) displays wild oscillations due to $\mathcal{P}(\vec{k})$. To mitigate this, the Magnitude of the FT (mag-FT) is taken, and the analysis proceeds by assuming that $\mathcal{P}(\vec{k})$ is approximately constant in magnitude so that $|\mathcal{P}(\vec{k})| \approx \bar{c}\sqrt{N}$, where \bar{c} is the average value of the c_j . The result of this procedure is illustrated in Figure 1(c), showing that debilitating noise still persists in the FT after taking the modulus. Moreover, the procedure of obtaining the mag-FT effectively eliminates half of the useful information in the complex-valued FT, annihilating all of the phase information from electron scattering processes originally present in real space. Intense peaks and contours in the real and imaginary parts of $\delta\rho(\vec{k}, \omega)$ are experimental indicators of dominant scattering wavevectors and order parameter symmetries, which can reveal important properties about the superconducting gap function sign structure [24, 25] and surface states of topological insulators [26, 27]. However, random phase noise fluctuations in experimental QPI spectra make comparisons with theoretical QPI calculations difficult [28].

An improved analysis technique to FT-STM would identify the location and the LDoS signature associated with each defect in a quantitatively-rigorous fashion that respects experimental and material-specific constraints. For instance, defects remain fixed in position

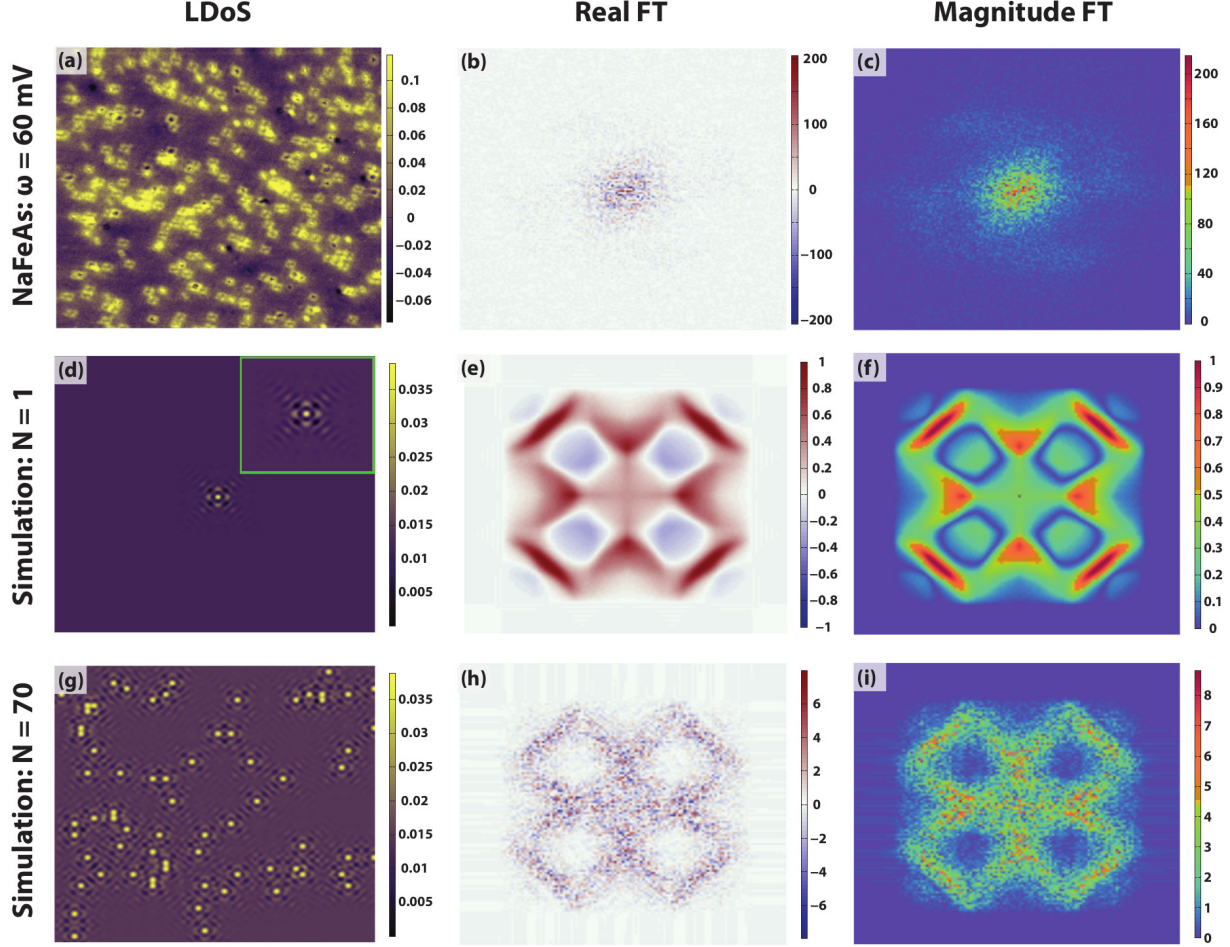


FIG. 1. Shortcomings of the Fourier transform analysis. (a) The experimentally-obtained LDoS of NaFeAs over a $100 \times 100 \text{ nm}^2$ area of the sample at energy $\omega = 60 \text{ mV}$ from Ref 6 with junction conditions $V = -100 \text{ mV}$ and $I = 300 \text{ pA}$ measured at $T = 26 \text{ K}$. (b)-(c) Real part and magnitude, respectively, of the FT of (a) showing large phase noise. (d) Simulated image of scattering from a single point defect. (e)-(f) Real part and magnitude, respectively, of the FT of (d). The LDoS scale in (d) was chosen such that the FT magnitude for the simulated single defect had a maximum of 1. (g)-(i) Corresponding simulated LDoS and FTs for scattering from 70 point defects that are randomly distributed in space. All FT spectra are shown for $-3\pi/5a \leq k_x, k_y \leq 3\pi/5a$. Comparison with the single defect case shows that noise in the FTs arises from the random placement of defects. Furthermore, the maximum amplitude of the FT scales approximately as \sqrt{N} , resulting in a loss of signal fidelity in the FT analysis.

across a series of STM images in which the measurement bias voltage is varied (see Figure 2). In this work, we present an analysis technique based on nonconvex optimization that possesses these desirable features while being broadly applicable to other forms of microscopy and image analysis.

Our algorithm is based on a deconvolutional procedure illustrated in Figure 2. The image (denoted as \mathcal{Y}) in Figure 2(a) was produced by simulating the effect of quasiparticle

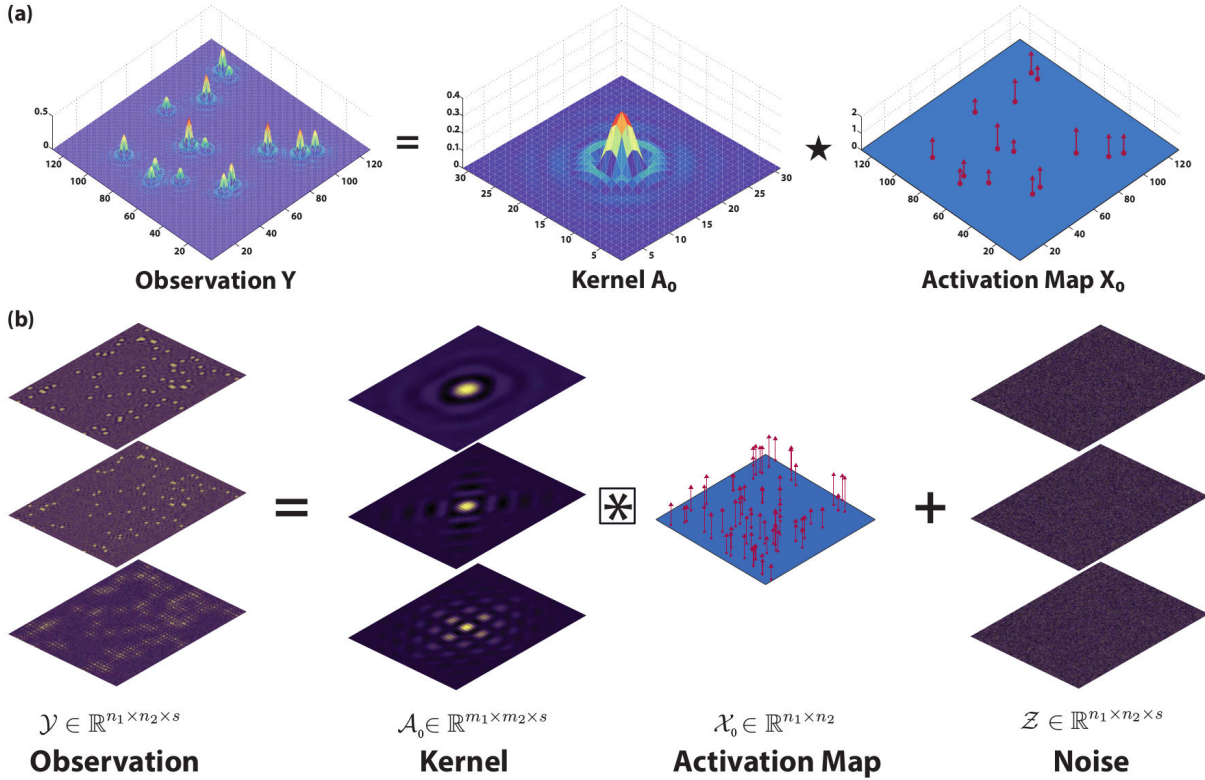


FIG. 2. Convolutional data model for STM. (a) Schematic representation of the convolutional data model $\mathcal{Y} = \mathcal{A}_0 \star \mathcal{X}_0$ for a noise-free simulated STM measurement. (b) Schematic representation of STM analysis as a high-dimensional deconvolution problem. Each constant-energy plane of \mathcal{A}_0 is convolved with the known activation map \mathcal{X}_0 and combined with additive noise \mathcal{Z} to produce the noisy observation \mathcal{Y} . Algorithms for SBD seek to efficiently estimate \mathcal{A}_0 and \mathcal{X}_0 given the noisy measurement \mathcal{Y} .

scattering from numerous point defects randomly distributed across the image. At a given bias voltage, the image consists of a recurrent scattering pattern (called the kernel \mathcal{A}_0) convolved with the locations and relative weights of each defect (called the activation map \mathcal{X}_0) as illustrated in Figure 2(a) and represented as $\mathcal{Y} = \mathcal{A}_0 \star \mathcal{X}_0$. The underlying challenge in our analysis is to invert the procedure – starting with an STM image, determine the kernel and its corresponding activation map. The kernel and activation map are easily identified by inspection in Figure 2(a), however this becomes a highly non-trivial problem in the presence of many overlapping kernels and experimental noise. Similar convolutional models are used in neuroscience to model neuron spike patterns [12] and in systems biology to capture responses of the endocrine system [13]. Hence an algorithm developed to solve this problem has broad applicability.

When \mathcal{A}_0 contains multiple slices, with each slice corresponding to a different bias voltage,

we mathematically express the proposed model for STM measurements by collecting the convolutions for each voltage slice using the notation

$$\mathcal{Y} = \mathcal{A}_0 \boxtimes \mathcal{X}_0 + \mathcal{Z}, \quad (3)$$

which is schematically depicted in Figure 2(b). The activation map \mathcal{X}_0 is shared globally across all measurement biases and \mathcal{Z} is an additive noise tensor. The task of recovering both \mathcal{A}_0 and \mathcal{X}_0 given \mathcal{Y} is known as the Sparse Blind Deconvolution (SBD) problem.

Over the last decade, a wealth of heuristics and applications for sparse signal recovery have been developed, often leading to efficient algorithms in theory as well as in practice [29, 30] (see Supplementary Information Section II). We investigate the following heuristic for producing estimates $\hat{\mathcal{A}}$ and $\hat{\mathcal{X}}$ for \mathcal{A}_0 and \mathcal{X}_0 , by posing an optimization problem based on (3):

$$\hat{\mathcal{A}} = \arg \min_{\mathcal{A}} \min_{\mathcal{X}} \left[\psi_{\lambda}(\mathcal{A}, \mathcal{X}) \equiv \frac{1}{2} \|\mathcal{A} \boxtimes \mathcal{X} - \mathcal{Y}\|_F^2 + \lambda r(\mathcal{X}) \right] \quad (4)$$

which allows one to recover $\hat{\mathcal{X}} = \arg \min_{\mathcal{X}} \psi_{\lambda}(\hat{\mathcal{A}}, \mathcal{X})$.

This is similar to previous formulations proposed for various SBD applications: the Frobenius norm term $\|\cdot\|_F^2$ promotes data fidelity upon minimization ($\mathcal{Y} \simeq \hat{\mathcal{A}} \boxtimes \hat{\mathcal{X}}$), and a regularization term $r(\hat{\mathcal{X}})$ is chosen, such as the ℓ_1 norm, so that the minimization encourages $\hat{\mathcal{X}}$ to be sparse, with $\lambda \geq 0$ governing the trade-off between the two objectives. However, most SBD applications focus on signal enhancement that uses the convolutional model as a rough guideline, leading to a weak notion of accurate estimation [31]. In contrast, the convolutional model fits naturally into the STM setting, in which robust, consistent results are paramount for scientific investigation. These considerations prompt a number of choices that are not emphasized in previous heuristics, such as the domain of \mathcal{A} , form of $r(\hat{\mathcal{X}})$, and refinement of the estimates.

In order to solve this optimization problem, we present the SBD-STM algorithm:

Algorithm 1 Complete SBD-STM Procedure

Input:

- Observation $\mathcal{Y} \in \mathbb{R}^{n_1 \times n_2 \times s}$, kernel size (m_1, m_2) , initial $\lambda_0 \geq 0$, decay rate $\alpha \in [0, 1)$, and final $\lambda_{\text{end}} \geq 0$.

Initial phase:

1. Randomly initialize: $\mathcal{A}^{(0)} \in \mathcal{S} = \mathbb{S}^{m_1 \times m_2 \times s}$.
2. $\mathcal{A}_*^{(0)}, \mathcal{X}_*^{(0)} \leftarrow \text{ASolve}(\mathcal{A}^{(0)}, \lambda_0, \mathcal{Y})$.

Refinement phase:

1. Lifting: Get $\mathcal{A}^{(1)} \in \mathcal{S}' = \mathbb{S}^{m_1' \times m_2' \times s}$ by zero-padding the edges of $\mathcal{A}_*^{(0)}$ with a border of width $\lfloor \frac{m_i}{2} \rfloor$.
2. Set $\lambda_1 = \lambda_0$.
3. Continuation: **Repeat** for $k = 1, 2, \dots$ **until** $\lambda_k \leq \lambda_{\text{end}}$,
 - (a) $\mathcal{A}_*^{(k)}, \mathcal{X}_*^{(k)} \leftarrow \text{ASolve}(\mathcal{A}^{(k)}, \lambda_k, \mathcal{Y}, \mathcal{X}_*^{(k-1)})$,
 - (b) Centering:
 - i. Find the size $m_1 \times m_2$ submatrix of $\mathcal{A}_*^{(k)}$ that maximizes the Frobenius (square) norm across all $m_1 \times m_2$ submatrices.
 - ii. Get $\mathcal{A}^{(k+1)}$ by shifting $\mathcal{A}_*^{(k)}$ so that the chosen $m_1 \times m_2$ restriction is in the center, removing and zeropadding entries as needed.
 - iii. Normalize $\mathcal{A}^{(k+1)}$ so it lies in \mathcal{S}' .
 - iv. Shift $\mathcal{X}_*^{(k)}$ along the anti-parallel vector to the shift of $\mathcal{A}_*^{(k)}$.
 - (c) Set $\lambda_{k+1} = \alpha \lambda_k$.

Output:

1. Extract $\hat{\mathcal{A}} \in \mathcal{S}$ by extracting the restriction of the final $\mathcal{A}^{(k+1)}$ to the center $m_1 \times m_2$ window.
2. Find the corresponding activation map $\hat{\mathcal{X}} \in \mathbb{R}^{n_1 \times n_2}$ by solving $\min_{\mathcal{X}} \psi_{\lambda_k}(\hat{\mathcal{A}}, \mathcal{X})$.

Function ASolve

Input:

- Current kernel, \mathcal{A}_{in} , current sparsity parameter, λ_{in} , the observation \mathcal{Y} , current activation map \mathcal{X}_{in} (Refinement Phase)

Minimization**if** Initial Phase **then** $\mathcal{X}_1 \leftarrow$ Minimize \mathcal{X} for $\psi_{\lambda_{in}}(\mathcal{A}_{in}, \mathcal{X})$ using the FISTA algorithm [32].**else** $\mathcal{X}_1 \leftarrow \mathcal{X}_{in}$ **end if**

1. $\mathcal{A}_{out} \leftarrow$ Minimize \mathcal{A} for $\psi_{\lambda_{in}}(\mathcal{A}, \mathcal{X}_1)$ using the Riemannian Trust-Region Method (RTRM) over the sphere [33].
2. $\mathcal{X}_{out} \leftarrow$ Minimize \mathcal{X} for $\psi_{\lambda_{in}}(\mathcal{A}_{out}, \mathcal{X})$ using FISTA.

Output:

- $\mathcal{A}_{out}, \mathcal{X}_{out}$.
-

See Supplementary Information Sections II and III for further discussion on formulating and solving (4), and Section IV for how our approach to SBD can be applied to image

deblurring by using an objective similar to (4).

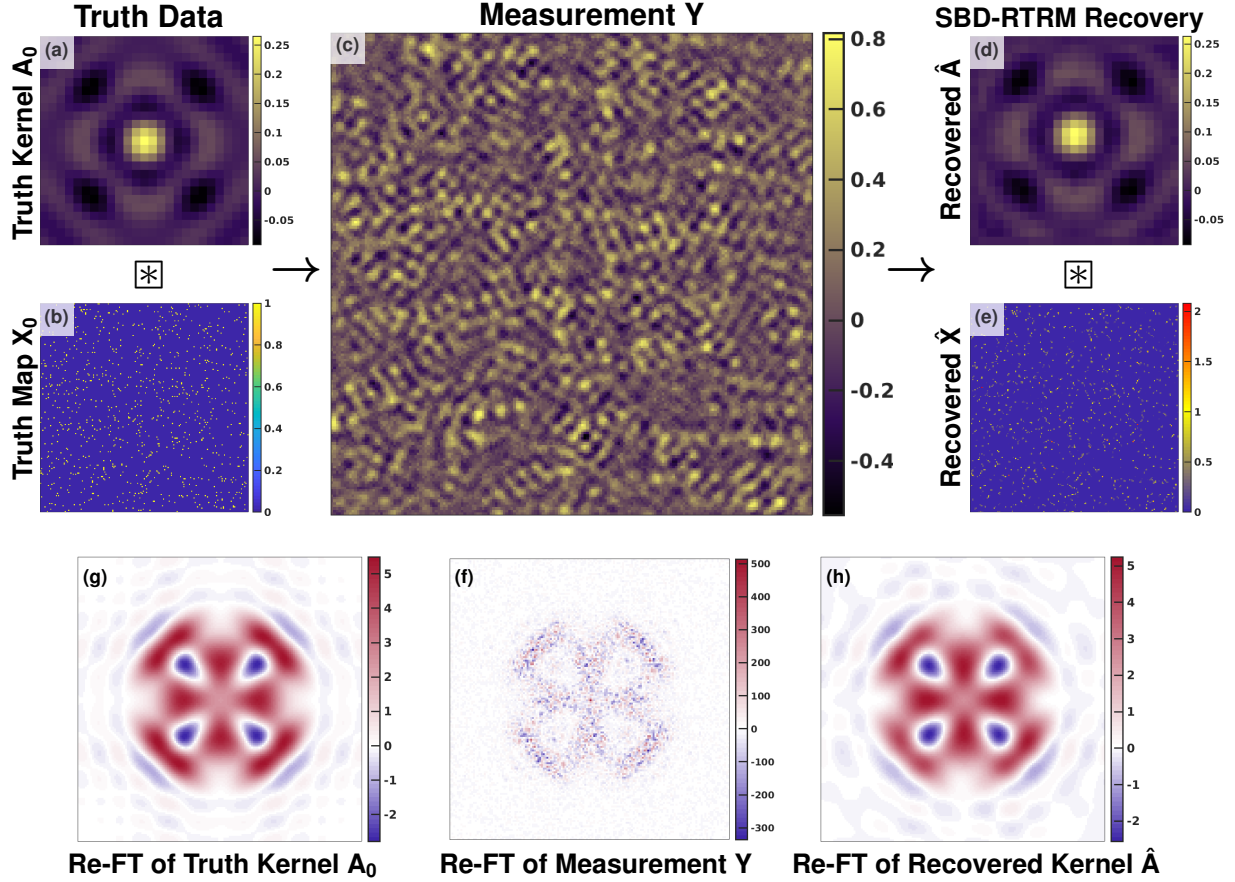


FIG. 3. Illustrating the SBD-STM procedure. The simulated kernel (size 25×25 pixels) in (a) is convolved with the activation map in (b) and added to random noise with $\text{SNR} \approx 0.792$ to produce the simulated noisy measurement shown in (c). The simulated measurement is a 185×185 pixel image with a defect concentration of $\theta = 2.73\%$. (d) Recovered kernel and (e) recovered activation map obtained using SBD-STM with $\lambda = 0.1$, showing excellent agreement with simulation inputs in (a) and (b). The Re-FTs of the truth kernel, noisy measurement, and the recovered kernel from SBD-STM, shown in panels (f), (g), and (h), respectively. The Re-FT spectra are all shown with $-3\pi/5a \leq k_x, k_y \leq 3\pi/5a$. The SBD-STM based FT shows both vastly improved SNR and a phase-sensitive recovery of the scattering interference.

To demonstrate the strength of SBD-STM, consider the situation illustrated in Figure 3. We generated a simulated observation \mathcal{Y} using a ground truth scattering pattern \mathcal{A}_0 similar to Figure 1(d) and a dense, randomly generated activation map \mathcal{X}_0 shown in Figure 3(b). Convolution of the truth data with the activation map and adding significant white noise with variance η so that the Signal-to-Noise Ratio (SNR) is less than unity, with $\text{SNR} \equiv \frac{\text{var}(\mathcal{A}_0)}{\eta}$, we generate the image shown in Figure 3(c). With many overlapping kernels and substantial noise, it is a futile task to accurately identify the underlying kernel and activation map

of the image through visual inspection. However, as shown in Figure 3(d)-(e), SBD-STM successfully recovers a kernel $\hat{\mathcal{A}}$ and its associated activation map $\hat{\mathcal{X}}$ that closely resemble the truth data. The results shown in Figure 3 were obtained with a fixed $\lambda = 0.1$. The scaling of the activation map entries is due to the choice of λ , and the noise also introduces blurring in the activation map [34]. Despite this, the overall features of the activation map and the recovered kernel are remarkably similar to the ground truth.

In Fourier space, the Re-FT of \mathcal{Y} is missing crucial features of the true Re-FT spectrum and has noise fluctuations ≈ 100 times that of the true transform. However, the Re-FT of the SBD-STM recovered kernel is consistent with the true Re-FT in both its structure and amplitude.

In our implementation, SBD-STM yields an activation map shared across all bias voltages. This not only reveals the spatial distribution of the defect kernels, but also naturally improves the accuracy of the SBD-STM recovered kernels at bias energies with noisy measurements. Consequently, SBD-STM returns more physically meaningful results when data from multiple biases are simultaneously analyzed than if each constant-bias slice of \mathcal{Y} were individually analyzed. SBD-STM results on a simulated noisy STM dataset with 41 bias voltages are found in Supplementary Information Section V, demonstrating that SBD-STM is successful in optimizing the objective function with STM constraints in mind.

Before invoking SBD-STM on experimental data, we must understand its limitations and domain of applicability. The complexity of the STM deconvolution problem varies depending on the SNR and the overlap tendency of nearby defects. A series of numerical experiments on simulated data was performed to investigate the effects of defect concentration θ – the probability that any entry of \mathcal{X}_0 is “on” – and additive measurement noise on the expected success of SBD-STM. Simulated STM images are produced in a similar fashion as in Figure 3, and the performance of SBD-STM was assessed as a function of four adjustable parameters – the image size $n \equiv n_1 \times n_2$, kernel size $m \equiv m_1 \times m_2$, kernel concentration θ , and SNR. Details of the data generation and simulation work are contained in Supplementary Information Sections I and VI. To assess the accuracy of kernel recovery in real space, we define the real space recovery error metric as $\epsilon(\hat{\mathcal{A}}_{\theta,\eta}, \mathcal{A}_0) \equiv \frac{2}{\pi} \arccos \left| \langle \hat{\mathcal{A}}_{\theta,\eta}, \mathcal{A}_0 \rangle \right|$, with $\langle \hat{\mathcal{A}}_{\theta,\eta}, \mathcal{A}_0 \rangle$ denoting the inner product of the vectorizations of $\hat{\mathcal{A}}_{\theta,\eta}$ and \mathcal{A}_0 , which are the recovered and truth kernels, respectively. Figure 4(a) depicts a normalized defect size $\frac{m}{n}$ vs. concentration θ “phase diagram” to explore the interplay between $\frac{m}{n}$ and θ on real-space algorithmic accuracy

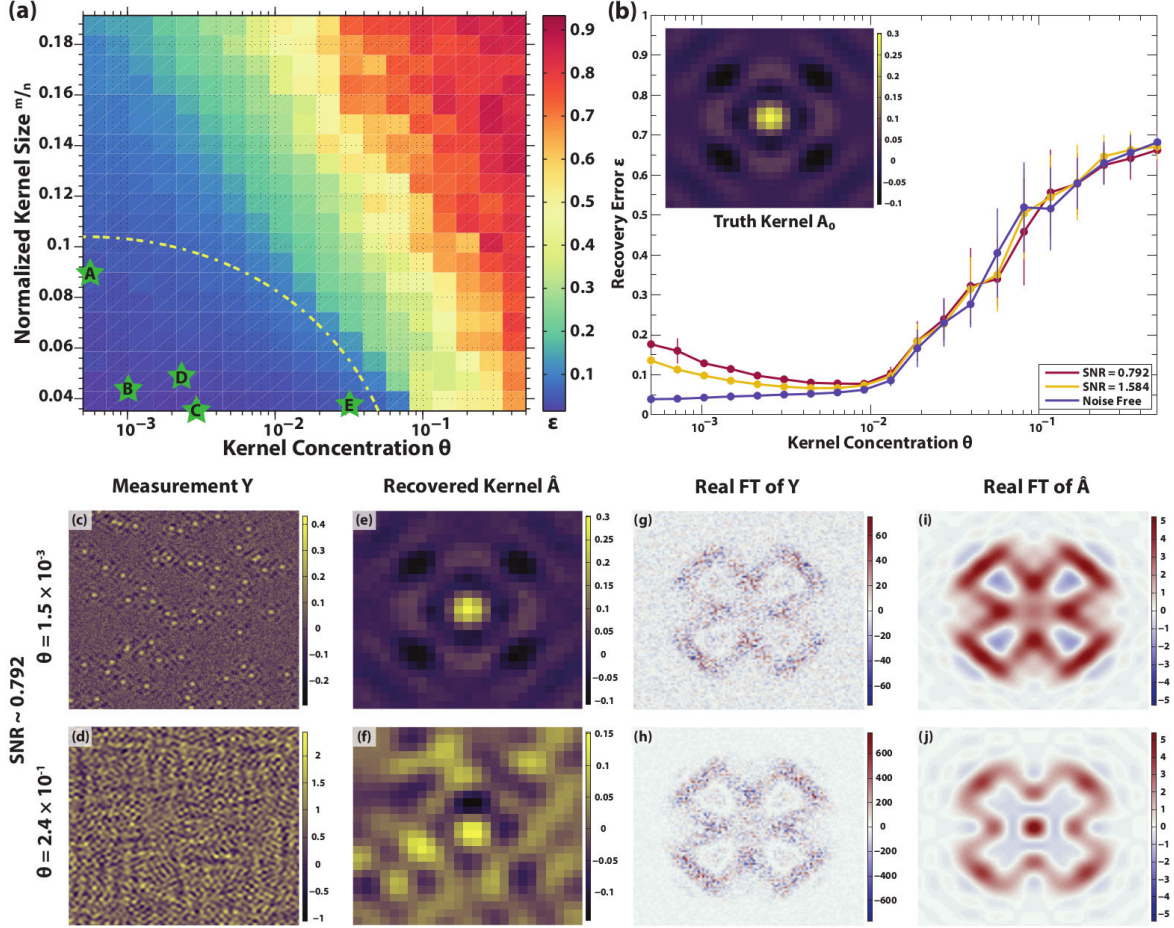


FIG. 4. Benchmarking SBD-STM performance. (a) SBD-STM performance phase diagram from noise-free simulated results on images of area $n = 256 \times 256$, plotting the error metric $\epsilon(\hat{\mathcal{A}}_{\theta, \eta}, \mathcal{A}_0)$ as a function of normalized kernel size and concentration θ (the number of defects scaled by the number of pixels). Each point on the diagram is determined from the mean of 20 independent simulated measurements. SBD-STM performs well in the blue regions, but begins to fail in the red regions, at very high kernel size or concentration. The region where typical STM measurements are performed is bounded by the dashed line and the lower and left axes. Green stars labeled A, B, C, D, and E indicate representative images from Refs. 3, 4, 6, 7, and 35, respectively. (b) Performance of SBD-STM in the presence of additive noise in the measurement at a fixed value of the normalized kernel size $m/n = 0.14$. (c)-(f) Examples of simulated measurements from panel (b) and their corresponding SBD-STM recovered kernels. (g)-(j) A comparison of the Re-FTs of the measurement and the SBD-STM recovered kernel, indicating that SBD-STM consistently outperforms FT-STM across all parameter ranges. All Re-FT spectra are shown with $-3\pi/5a \leq k_x, k_y \leq 3\pi/5a$.

$\epsilon(\hat{\mathcal{A}}_{\theta}, \mathcal{A}_0)$ in noise-free ($\eta = 0$) simulated measurements. We observe a phase transition in SBD-STM performance in the $\frac{m}{n} - \theta$ plane. The bottom-left of the plot captures situations in which the defects have negligible probability of overlapping, facilitating the near-perfect deconvolution of the noise free image. Increasing either $\frac{m}{n}$ or θ introduces error in the kernel

recovery due to increased overlapping between defects. Practically, $\frac{m}{n}$ can be reduced by increasing the overall STM measurement area n in an attempt to perform deconvolution-by-inspection. However at high defect concentrations θ or moderate noise levels, this strategy cannot guarantee success while SBD-STM can still return reliable estimates.

Next, we briefly discuss the SBD-STM performance as a function of noise in the signal. Figure 4(b) shows the evolution of $\epsilon(\hat{\mathcal{A}}_{\theta,\eta}, \mathcal{A}_0)$ as a function of defect concentration θ for three values of SNR ranging from noise free to noise-dominated (SNR = 0.792). At high noise levels, performance error fluctuations in the far left of the plot appear because of the statistically futile challenge of accurately identifying low-density, low-intensity motifs under high levels of noise. The error curves appear to converge into a narrow band when $\theta \gtrsim 0.01$, demonstrating that the algorithm is robust to a wide range of SNRs for higher concentrations. By $\theta \approx 0.2$, the defect concentrations are sufficiently dense so that virtually all defect kernels are overlapping, causing SBD-STM to collapse and return unreliable estimates. These trends persist when the kernel size and SNR are further increased, as described in Supplementary Information Section VI. Altogether, our simulations show that in the range of parameters where typical STM experiments are performed (bounded by the dashed line in Figure 4(a)), SBD-STM performs splendidly ($\epsilon < 0.1$) and consistently outperforms the usual FT-STM methodology even in the presence of considerable noise, as seen in Figure 4(c)-(j).

The results obtained above on synthetic data show that SBD-STM is able to recover kernels even at high defect density and in the presence of significant white noise, where alternate techniques such as manual detection fail. However, one might still question whether the method will work on real STM data, which might have other types of noise or errors which we have not accounted for in our synthetic data. In order to investigate this fully, we now apply SBD-STM to investigate a set of experimentally-obtained STM images of $\text{NaFe}_{1-x}\text{Co}_x\text{As}$ at different values of $x = 0.0, 0.015$ and 0.02 . At $x = 0.0$ (parent compound), no additional cobalt dopants are present in the lattice, and the only defects present are those intrinsic to the crystal, which are at a concentration of about 1%. This compound has been previously studied via STM and the data have been analyzed using the standard Fourier transform technique [6]. To contrast with the standard FT-STM analysis, we implement SBD-STM on raw experimental data to demonstrate the significant improvement in data fidelity of the Re-FT. Shown in figure 5 (b) and (c) are the recovered Kernel and activation map respectively from the map shown in (a). Figure 5 (d) and (e) show the Re-FT of

the entire image and of the kernel respectively over the same range in Fourier space. The phase sensitive recovery of the Fourier transform in Figure 5 (e) when compared to (d) is immediately apparent. We note that for this particular doping the individual kernels are well separated, and the kernel can be isolated directly by eye from the large area image in Figure 5(a). We show the application of SBD-STM to this sample to illustrate that the recovered kernel is indeed what one would expect by direct measurement around an individual defect.

We now turn to the sample with $x = 0.015$, a STS image of which is shown in Figure 5(f). At this doping, we see that there are regions of high-density clustering of the kernels, where the clustering is dense enough such that the individual kernels overlap and become difficult to resolve. In Figure 5(g) and (h), we show the corresponding recovery for the kernel and activation map respectively. The Re-FT of the entire map and the recovered kernel are shown in Figure 5(i) and (j) respectively. At this defect level, we can very occasionally see isolated defects, and the recovered kernel is seen to nicely match with the differential conductance around these isolated defects.

Finally, we consider a sample that is optimally doped (highest T_c) with a nominal cobalt concentration of $x = 0.02$. Shown in Figure 5(k) is an STS image obtained on this sample at $T = 5.9$ K. At this doping level, there are no isolated impurities present anywhere in the sample, and the kernel can not be manually recovered. The SBD-STM is able to recover the kernel and activation map as shown in Figure 5(l) and (m) respectively. The Re-FT of the entire image and of the recovered kernel are shown in Figure 5(n) and (o) respectively. We see from the series of data in Figure 5 that SBD-STM works over the entire doping range that is relevant to STM experiments and is able to recover high-quality kernels with phase-sensitive Fourier transforms. As a side benefit of SBD-STM, we can obtain more accurate defect or dopant counts from the recovered activation maps.

From the results shown on both synthetic and real experimental STM data, we can see that SBD-STM provides a complete recovery of kernels in real space and therefore a phase sensitive recovery of the Fourier transform in reciprocal space. Within the formulation of quasiparticle interference, the phase of the Fourier transform in the QPI signal is dependent on the incoming and outgoing quasiparticle's Green's function as well as the potential of the impurity. The availability of phase information can give us new insight into individual materials that is not available simply from the magnitude of the QPI signal. In the re-

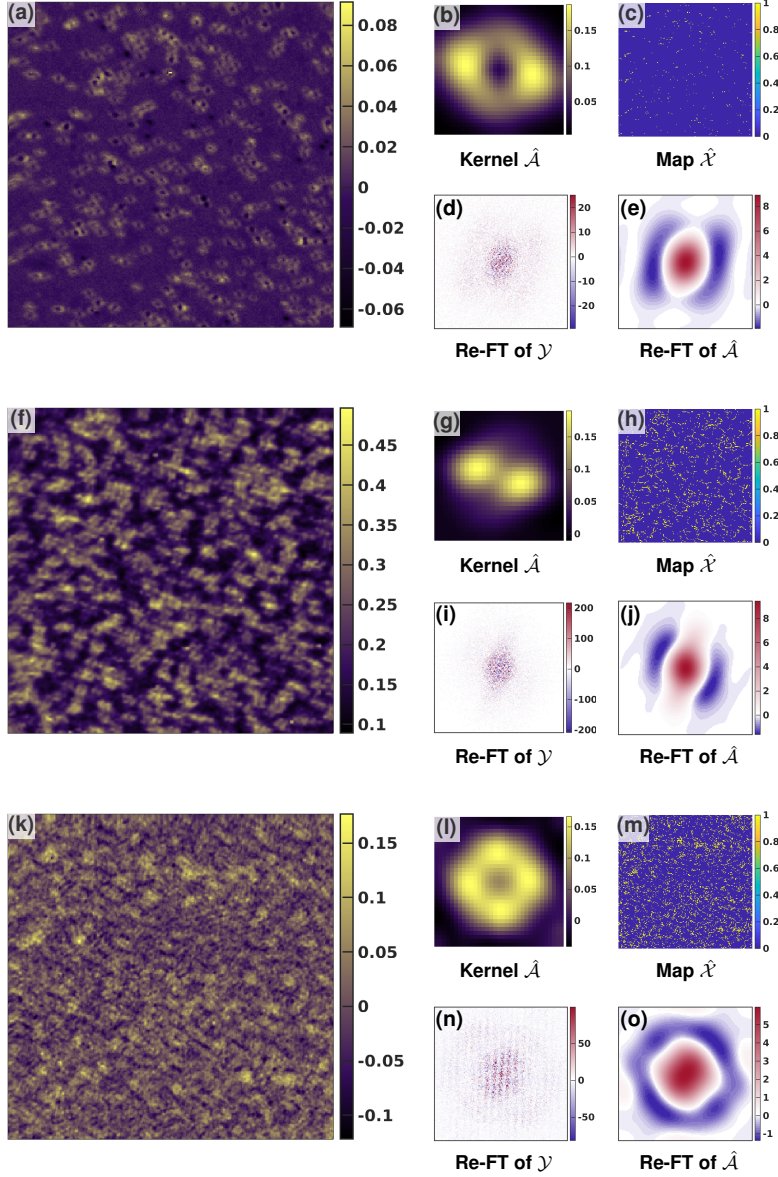


FIG. 5. SBD-STM recoveries with increasing density of defects. In the left column, we have conductance maps with Co defects in $\text{NaFe}_{1-x}\text{Co}_x\text{As}$ of (a) high-quality ($T = 71$ K, $I = 59$ pA, $V_{set} = -100$ mV, 114×114 nm), (f) $x = 0.015$ ($T = 6$ K, $I = -200$ pA, $V_{set} = -20$ mV, 50.4×50.4 nm), and (k) $x = 0.02$ ($T = 5.9$ K, $I = 200$ pA, $V_{set} = -50$ mV, 250×250 nm) biased at energies of (a) 40 meV, (f) 5 meV, and (k) -7 meV. In the right column, clockwise from the top left, we have the recovered kernel (b,g,l), the recovered activation map (c,h,m), the Re-FT of the kernel (d,i,n), and the Re-FT of the conductance map (e,j,o), for comparison. The recovered kernels have been given 2-fold rotational symmetry, and all activations have been set to 1 to make them more readily visible.

mainder of this paper, we consider one such new insight into the physics of $\text{NaFe}_{1-x}\text{Co}_x\text{As}$.

NaFe_{1-x}Co_xAs, like many of the pnictides displays a superconducting dome as a function of cobalt doping. The maximum T_c at optimal doping ($x = 0.02$) reaches 18 K. As with the other pnictides, determining the symmetry of the superconducting order parameter in this compound is of much current interest. In this context, recent theoretical work on QPI in the superconducting state of the pnictides [36, 37] has opened up the possibility of distinguishing different superconducting order parameters from their QPI signature under the assumption that interband scattering in the superconducting state dominates the QPI signal. In [36], the (real) Fourier transform of the QPI signal around a single defect $\delta\rho(\vec{q}, \omega)$ is integrated over momentum to produce the quantity $\delta\rho(\omega)$. This quantity is then anti-symmetrized with respect to energy relative to the Fermi level to produce a quantity $\delta\rho^-(\omega) = \delta\rho(\omega) - \delta\rho(-\omega)$. It is shown in [36] that in the case of s^\pm pairing, $\delta\rho^-(\omega)$ is large and of constant sign over the energy range near the superconducting gap. Conversely, in the case of s^{++} pairing, $\delta\rho^-(\omega)$ is expected to be small and have a sign change around the gap energy. In order to carry out the integration over \vec{q} described in this procedure, it is required that we have access to the phase of the QPI signal. One way of achieving this is to directly image around an isolated dopant or defect where the complete phase sensitive pattern can be measured. Such STS imaging has recently been performed on iron chalcogenides [38, 39]. However, this method has not been applied to the iron arsenides, especially at optimal doping where the defect or dopant density is high and the phase information in the FT was not previously available. Armed with the phase-sensitivity of SBD-STM, we now analyze differential conductance maps of near optimally doped NaFe_{1-x}Co_xAs to investigate the superconducting order parameter at optimal doping.

We start with a dataset that consists of 21 raw STS images from -10 meV to +10 meV in 1 meV increments on an optimally doped NaFe_{1-x}Co_xAs sample at T=5.9 K. One of these raw images at $\omega = -10$ meV is shown in Figure 6(a). Notice that no individual motifs can be resolved by eye. We then proceed to recover the kernels $\hat{\mathcal{A}}(\vec{r}, \omega)$ at each energy using SBD-STM. An example of this recovery is shown in Figure 6(b), which is the recovered SBD-STM kernel $\hat{\mathcal{A}}(r, \omega = -10 \text{ meV})$, recovered from the raw STS image in Figure 6(a). The recovered kernel lacks the strong anisotropy of recovered kernels from the underdoped regime, suggesting that electronic nematicity is not strong at this doping. Assuming that SBD-STM has worked correctly, the recovered $\hat{\mathcal{A}}(\vec{r}, \omega)$ is identical to the real space QPI signal $\delta\rho(\vec{r}, \omega)$. We then take the real-part of the 2-D Fourier transform $\hat{\mathcal{A}}(\vec{q}, \omega)$, as shown

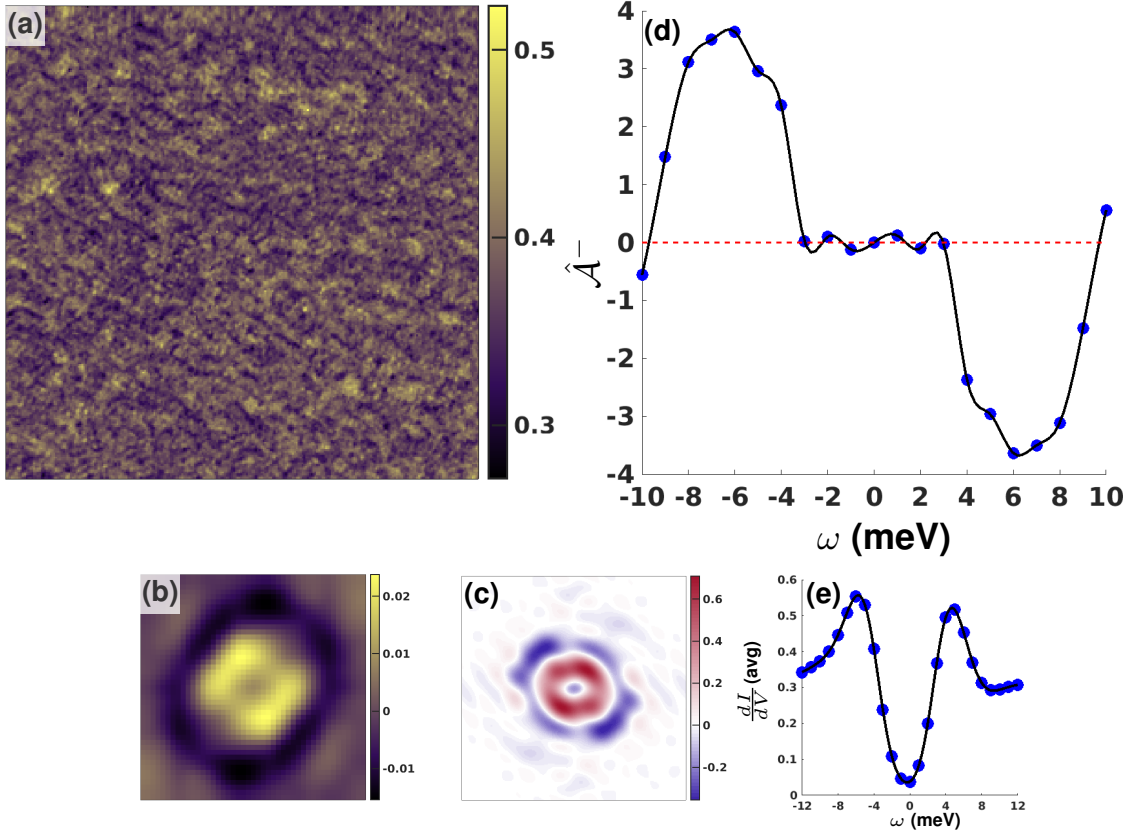


FIG. 6. (a) Differential conductance map at $\omega = -10$ meV for an optimally doped $\text{NaFe}_{1-x}\text{Co}_x\text{As}$ sample ($x=0.02$), over a $250 \text{ nm} \times 250 \text{ nm}$ field of view with $T = 5.9 \text{ K}$, $I = 200 \text{ pA}$, and $V_{set} = -50$ meV. b) recovered kernel, $\hat{\mathcal{A}}$, from the conductance map in a). c) Fourier transform of the recovered kernel. d) $\hat{\mathcal{A}}^-(\omega)$, computed from the recovered kernels. The large and constant sign of the response is an indication of s^\pm pairing. e) Spatially averaged differential conductance from the same area as a function of energy, revealing the superconducting gap $2\Delta = 11$ meV.

in Figure 6(c) at $\omega = -10$ meV. This FT has the full phase information present, and we can then integrate over \vec{q} and antisymmetrize with respect to energy:

$$\hat{\mathcal{A}}^-(\omega) = \sum_{\vec{q}} \text{Re}(\hat{\mathcal{A}}(\vec{q}, \omega)) - \text{Re}(\hat{\mathcal{A}}(\vec{q}, -\omega))$$

We perform this procedure at each energy, and plot the resultant $\hat{\mathcal{A}}^-(\omega)$ in Figure 6(d). In (e), we show the spatially averaged differential conductance from the same data sets as a function of energy, revealing the superconducting gap. From the two coherence peaks,

we calculate a 2Δ of 11 meV. We can clearly see from Figure 6(d) that $\hat{\mathcal{A}}^-(\omega)$ is peaked near the superconducting gap, and has no sign change in the energy range near the gap, as expected for an s^\pm order parameter. This procedure illustrates some of the new physical insight into STS image data that can be obtained once the complete phase information in the QPI signal is available for analysis.

In its current implementation, SBD-STM addresses the problem of identifying a single motif across a series of images. Beyond the identification of real space motifs in microscopy images, SBD-STM can also be applied to problems in which the motif is sparse in the appropriately chosen space, such as sparsity in the spatial gradient for natural image deblurring [40, 41]. Moreover, the flexibility of the convolutional data model in (3) affords the natural generalization, $\mathcal{Y} = \sum_{j=1}^M \mathcal{A}_0^{(j)} \boxtimes \mathcal{X}_0^{(j)} + \mathcal{Z}$, which expands the scope of SBD-STM to identify multiple distinct kernels in any series of images. In particular, STM images that contain various short-range orders, such as charge or spin density waves, would be amenable to a similar analysis [7, 35, 42–44]. SBD-STM recovered results from these STM measurements can be directly compared with theoretical predictions [45–47] to understand the nature of competing orders in superconductors and other strongly correlated materials. Other analysis methodologies [42, 44, 48] have been recently proposed to improve FT data fidelity and provide some phase-sensitive information on the structure of ordered phases. These alternative approaches provide compelling information under suitable conditions, but their results are still vulnerable to phase noise contamination. The correct implementation of SBD-STM to such cases remains an open but solvable problem.

We thank Ethan Rosenthal and Erick Andrade for help with STM data acquisition, and Andrew Millis and Rafael Fernandes for discussions. This work is supported by the National Science Foundation Bigdata program (Grant number IIS-1546411). Support for STM equipment and operations is provided by the Air Force Office of Scientific Research (Grant number FA9550-16-1-0601).

-
- [1] M. F. Crommie, C. P. Lutz, and D. M. Eigler, “Imaging standing waves in a two-dimensional electron gas,” *Nature* **363**, 524–527 (1993).
 - [2] J. E. Hoffman, K. McElroy, D.-H. Lee, K. M. Lang, H. Eisaki, S. Uchida, and J. C. Davis,

- “Imaging quasiparticle interference in $\text{Bi}_2\text{Sr}_2\text{CaCu}_2\text{O}_{8+x}$,” *Science* **297**, 1148–1151 (2002).
- [3] G. M. Rutter, J. N. Crain, N. P. Guisinger, T. Li, P. N. First, and J. A. Stroscio, “Scattering and interference in epitaxial graphene,” *Science* **317**, 219–222 (2007).
- [4] Pedram Roushan, Jungpil Seo, Colin V. Parker, Y. S. Hor, D. Hsieh, Dong Qian, Anthony Richardella, M. Z. Hasan, R. J. Cava, and Ali Yazdani, “Topological surface states protected from backscattering by chiral spin texture,” *Nature* **460**, 1106–1109 (2009).
- [5] T. Hanaguri, S. Niitaka, K. Kuroki, and H. Takagi, “Unconventional s-wave superconductivity in $\text{Fe}(\text{Se},\text{Te})$,” *Science* **328**, 474–476 (2010).
- [6] Ethan P. Rosenthal, Erick F. Andrade, Carlos J. Arguello, Rafael M. Fernandes, Ling Y. Xing, X. C. Wang, C. Q. Jin, Andrew J. Millis, and Abhay N. Pasupathy, “Visualization of electron nematicity and unidirectional antiferroic fluctuations at high temperatures in NaFeAs ,” *Nature Physics* **10**, 225–232 (2014).
- [7] C. J. Arguello, E. P. Rosenthal, E. F. Andrade, W. Jin, P. C. Yeh, N. Zaki, S. Jia, R. J. Cava, R. M. Fernandes, A. J. Millis, T. Valla, R. M. Osgood, and A. N. Pasupathy, “Quasiparticle interference, quasiparticle interactions, and the origin of the charge density wave in 2H-nbse_2 ,” *Phys. Rev. Lett.* **114**, 037001 (2015).
- [8] Qiang-Hua Wang and Dung-Hai Lee, “Quasiparticle scattering interference in high-temperature superconductors,” *Phys. Rev. B* **67**, 020511 (2003).
- [9] Gregory A. Fiete and Eric J. Heller, “*Colloquium* : Theory of quantum corrals and quantum mirages,” *Rev. Mod. Phys.* **75**, 933–948 (2003).
- [10] S. A. Kivelson, I. P. Bindloss, E. Fradkin, V. Oganesyan, J. M. Tranquada, A. Kapitulnik, and C. Howald, “How to detect fluctuating stripes in the high-temperature superconductors,” *Rev. Mod. Phys.* **75**, 1201–1241 (2003).
- [11] K. McElroy, R. W. Simmonds, J. E. Hoffman, D. H. Lee, J. Orenstein, H. Eisaki, S. Uchida, and J. C. Davis, “Relating atomic-scale electronic phenomena to wave-like quasiparticle states in superconducting $\text{Bi}_2\text{Sr}_2\text{CaCu}_2\text{O}_{8+\delta}$,” *Nature* **422**, 592–596 (2003).
- [12] Jonathan W. Pillow, Jonathon Shlens, E. J. Chichilnisky, and Eero P. Simoncelli, “A model-based spike sorting algorithm for removing correlation artifacts in multi-neuron recordings,” *PLoS ONE* **8**, e62123 (2013).
- [13] Rose T. Faghih, Munther A. Dahleh, Gail K. Adler, Elizabeth B. Klerman, and Emery N. Brown, “Deconvolution of serum cortisol levels by using compressed sensing,” *PLoS ONE* **9**,

- e85204 (2014).
- [14] Eric Betzig, George H. Patterson, Rachid Sougrat, O. Wolf Lindwasser, Scott Olenych, Juan S. Bonifacino, Michael W. Davidson, Jennifer Lippincott-Schwartz, and Harald F. Hess, “Imaging intracellular fluorescent proteins at nanometer resolution,” *Science* **313**, 1642–1645 (2006).
 - [15] David A. Muller, “Structure and bonding at the atomic scale by scanning transmission electron microscopy,” *Nat Mater* **8**, 263–270 (2009).
 - [16] G. Binnig and H. Rohrer, “Surface imaging by scanning tunneling microscopy,” *Ultramicroscopy* **1**, 157 – 160 (1983).
 - [17] C. Hanneken, F. Otte, A. Kubetzka, B. Dupe, N. Romming, K. von Bergmann, R. Wiesendanger, and S. Heinze, “Electrical detection of magnetic skyrmions by tunnelling non-collinear magnetoresistance,” *Nature Nanotechnology* **10**, 1039–1042 (2015).
 - [18] Mostafa Enayat, Zhixiang Sun, Udai Raj Singh, Ramakrishna Aluru, Stefan Schmaus, Alexander Yaresko, Yong Liu, Chengtian Lin, Vladimir Tsurkan, Alois Loidl, Joachim Deisenhofer, and Peter Wahl, “Real-space imaging of the atomic-scale magnetic structure of Fe_1Te ,” *Science* **345**, 653–656 (2014).
 - [19] Koji Kimoto, Keiji Kurashima, Takuro Nagai, Megumi Ohwada, and Kazuo Ishizuka, “Assessment of lower-voltage {TEM} performance using 3d fourier transform of through-focus series,” *Ultramicroscopy* **121**, 31 – 37 (2012).
 - [20] J.S. Jaffe and R.M. Glaeser, “Difference fourier analysis of surface features of bacteriorhodopsin using glucose-embedded and frozen-hydrated purple membrane,” *Ultramicroscopy* **23**, 17 – 28 (1987).
 - [21] F. Vonau, D. Aubel, G. Gewinner, S. Zabrocki, J. C. Peruchetti, D. Bolmont, and L. Simon, “Evidence of hole-electron quasiparticle interference in ErSi_2 semimetal by fourier-transform scanning tunneling spectroscopy,” *Phys. Rev. Lett.* **95**, 176803 (2005).
 - [22] L. Simon, F. Vonau, and D. Aubel, “A phenomenological approach of joint density of states for the determination of band structure in the case of a semi-metal studied by ft-sts,” *Journal of Physics: Condensed Matter* **19**, 355009 (2007).
 - [23] Fa Wang and Dung-Hai Lee, “The electron-pairing mechanism of iron-based superconductors,” *Science* **332**, 200–204 (2011).
 - [24] T. Hanaguri, Y. Kohsaka, M. Ono, M. Maltseva, P. Coleman, I. Yamada, M. Azuma, M. Takano, K. Ohishi, and H. Takagi, “Coherence factors in a high- T_c cuprate probed by

- quasi-particle scattering off vortices,” *Science* **323**, 923–926 (2009).
- [25] Shun Chi, S. Johnston, G. Levy, S. Grothe, R. Szedlak, B. Ludbrook, Ruixing Liang, P. Dosanjh, S. A. Burke, A. Damascelli, D. A. Bonn, W. N. Hardy, and Y. Pennec, “Sign inversion in the superconducting order parameter of lifeas inferred from bogoliubov quasiparticle interference,” *Phys. Rev. B* **89**, 104522 (2014).
- [26] Tong Zhang, Peng Cheng, Xi Chen, Jin-Feng Jia, Xucun Ma, Ke He, Lili Wang, Haijun Zhang, Xi Dai, Zhong Fang, Xincheng Xie, and Qi-Kun Xue, “Experimental demonstration of topological surface states protected by time-reversal symmetry,” *Phys. Rev. Lett.* **103**, 266803 (2009).
- [27] Yoshinori Okada, Chetan Dhital, Wenwen Zhou, Erik D. Huemiller, Hsin Lin, S. Basak, A. Bansil, Y.-B. Huang, H. Ding, Z. Wang, Stephen D. Wilson, and V. Madhavan, “Direct observation of broken time-reversal symmetry on the surface of a magnetically doped topological insulator,” *Phys. Rev. Lett.* **106**, 206805 (2011).
- [28] P. J. Hirschfeld, D. Altenfeld, I. Eremin, and I. I. Mazin, “Robust determination of the superconducting gap sign structure via quasiparticle interference,” *Phys. Rev. B* **92**, 184513 (2015).
- [29] E. J. Candes and T. Tao, “Decoding by linear programming,” *IEEE Transactions on Information Theory* **51**, 4203–4215 (2005).
- [30] M. Elad, “Sparse and redundant representation modeling - what next?” *IEEE Signal Processing Letters* **19**, 922–928 (2012).
- [31] A. Levin, Y. Weiss, F. Durand, and W. T. Freeman, “Understanding and evaluating blind deconvolution algorithms,” in [2009 IEEE Conference on Computer Vision and Pattern Recognition](#) (2009) pp. 1964–1971.
- [32] Amir Beck and Marc Teboulle, “A fast iterative shrinkage-thresholding algorithm for linear inverse problems,” *SIAM Journal on Imaging Sciences* **2**, 183–202 (2009), <https://doi.org/10.1137/080716542>.
- [33] P.-A. Absil, C.G. Baker, and K.A. Gallivan, “Trust-region methods on riemannian manifolds,” *Foundations of Computational Mathematics* **7**, 303–330 (2007).
- [34] Emmanuel J. Candès, Michael B. Wakin, and Stephen P. Boyd, “Enhancing sparsity by reweighted l_1 minimization,” *Journal of Fourier Analysis and Applications* **14**, 877–905 (2008).
- [35] M. P. Allan, T-M. Chuang, F. Masee, Yang Xie, Ni Ni, S. L. Bud’ko, G. S. Boebinger,

- Q. Wang, D. S. Dessau, P. C. Canfield, M. S. Golden, and J. C. Davis, “Anisotropic impurity states, quasiparticle scattering and nematic transport in underdoped $\text{Ca}(\text{Fe}_{1-x}\text{Co}_x)_2\text{As}_2$,” *Nature Physics* **9**, 220–224 (2013).
- [36] P. J. Hirschfeld, D. Altenfeld, I. Eremin, and I. I. Mazin, “Robust determination of the superconducting gap sign structure via quasiparticle interference,” *Phys. Rev. B* **92**, 184513 (2015).
- [37] Johannes H. J. Martiny, Andreas Kreisel, P. J. Hirschfeld, and Brian M. Andersen, “Robustness of a quasiparticle interference test for sign-changing gaps in multiband superconductors,” *Phys. Rev. B* **95**, 184507 (2017).
- [38] P. O. Sprau, A. Kostin, A. Kreisel, A. E. Böhmer, V. Taufour, P. C. Canfield, S. Mukherjee, P. J. Hirschfeld, B. M. Andersen, and J. C. Séamus Davis, “Discovery of orbital-selective cooper pairing in FeSe ,” *Science* **357**, 75–80 (2017), <http://science.sciencemag.org/content/357/6346/75.full.pdf>.
- [39] Zengyi Du, Xiong Yang, Dustin Altenfeld, Qiangqiang Gu, Huan Yang, Ilya Eremin, Peter J. Hirschfeld, Igor I. Mazin, Hai Lin, Xiyu Zhu, and Hai-Hu Wen, “Sign reversal of the order parameter in $(\text{Li}_1-x\text{Fex})\text{OHFe}_1\text{-yZn}_y\text{Se}$,” *Nature Physics* **14**, 134 EP – (2017).
- [40] Rob Fergus, Barun Singh, Aaron Hertzmann, Sam T. Roweis, and William T. Freeman, “Removing camera shake from a single photograph,” *ACM Trans. Graph.* **25**, 787–794 (2006).
- [41] A. Levin, Y. Weiss, F. Durand, and W. Freeman, “Understanding blind deconvolution algorithms,” *IEEE Transactions on Pattern Analysis and Machine Intelligence* **33**, 2354–2367 (2011).
- [42] Kazuhiro Fujita, Mohammad H. Hamidian, Stephen D. Edkins, Chung Koo Kim, Yuhki Kohsaka, Masaki Azuma, Mikio Takano, Hidenori Takagi, Hiroshi Eisaki, Shin-ichi Uchida, Andrea Allais, Michael J. Lawler, Eun-Ah Kim, Subir Sachdev, and J. C. Samus Davis, “Direct phase-sensitive identification of a d-form factor density wave in underdoped cuprates,” *Proceedings of the National Academy of Sciences* **111**, E3026–E3032 (2014).
- [43] Peng Cai, Xiaodong Zhou, Wei Ruan, Aifeng Wang, Xianhui Chen, Dung-Hai Lee, and Yayu Wang, “Visualizing the microscopic coexistence of spin density wave and superconductivity in underdoped $\text{NaFe}_{1-x}\text{Co}_x\text{As}$,” *Nature Communications* **4**, 1596 (2013).
- [44] M. H. Hamidian, S. D. Edkins, Chung Koo Kim, J. C. Davis, A. P. Mackenzie, H. Eisaki, S. Uchida, M. J. Lawler, E.-A. Kim, S. Sachdev, and K. Fujita, “Atomic-scale electronic

- structure of the cuprate d-symmetry form factor density wave state,” *Nature Physics* **12**, 150–156 (2016).
- [45] J. Knolle, I. Eremin, A. Akbari, and R. Moessner, “Quasiparticle interference in the spin-density wave phase of iron-based superconductors,” *Phys. Rev. Lett.* **104**, 257001 (2010).
- [46] Yuxuan Wang, Daniel F. Agterberg, and Andrey Chubukov, “Coexistence of charge-density-wave and pair-density-wave orders in underdoped cuprates,” *Phys. Rev. Lett.* **114**, 197001 (2015).
- [47] Yoni Schattner, Max H. Gerlach, Simon Trebst, and Erez Berg, “Competing orders in a nearly antiferromagnetic metal,” *Phys. Rev. Lett.* **117**, 097002 (2016).
- [48] Emanuele G. Dalla Torre, Yang He, and Eugene Demler, “Holographic maps of quasiparticle interference,” *Nature Physics* **12**, 1052–1056 (2016).

Dictionary Learning in Fourier Transform Scanning Tunneling Spectroscopy - Supplementary Information

Sky C. Cheung ^{a,1} John Y. Shin ^{a,1} Yenson Lau,² Zhengyu Chen,² Ju Sun,² Yuqian Zhang,² John N. Wright,^{2,†} and Abhay N. Pasupathy^{1,‡}

¹*Department of Physics, Columbia University, New York, NY 10027 USA*

²*Department of Electrical Engineering,
Columbia University, New York, NY 10027 USA*

(Dated: July 30, 2018)

arXiv:1807.10752v1 [physics.comp-ph] 19 Jul 2018

^a These authors contributed equally to this work

[†] johnwright@ee.columbia.edu

[‡] pasupathy@phys.columbia.edu

Supplementary Table I. Summary of symbols and notation

Symbol	Description
\vec{x}	position: \mathbb{R}^2
\vec{k}	wavevector (Fourier dual to \vec{x}): \mathbb{R}^2
ω	energy level (applied bias voltage): \mathbb{R}
$\rho(\vec{x}, \omega)$	LDoS/QPI map: $\mathbb{R}^2 \times \mathbb{R} \rightarrow \mathbb{R}$
$\rho_0(\vec{x}, \omega)$	LDoS/QPI map of an isolated defect: $\mathbb{R}^2 \times \mathbb{R} \rightarrow \mathbb{R}$
$\delta\rho(\vec{x}, \omega), \delta\rho_0(\vec{x}, \omega)$	local variation of LDoS: $\mathbb{R}^2 \times \mathbb{R} \rightarrow \mathbb{R}$
$n \equiv n_1 \times n_2$	number of pixels in an $n_1 \times n_2$ measurement/image: \mathbb{N}
$m \equiv m_1 \times m_2$	number of pixels in an $m_1 \times m_2$ kernel: \mathbb{N}
s	number of observed energy levels (bias voltages): \mathbb{N}
\mathcal{Y}	observation of LDoS signature on a finite grid: $\mathbb{R}^{n_1 \times n_2 \times s}$
\mathcal{A}	kernel (from a single defect) on the grid: $\mathbb{R}^{m_1 \times m_2 \times s}$
\mathcal{X}	activation map on the grid: $\mathbb{R}^{n_1 \times n_2}$
\mathcal{Z}	additive noise
\boxtimes	convolution operator between each kernel slice and the activation map
Hat: $\hat{\mathcal{A}}, \hat{\mathcal{X}}, \dots$	estimates of the corresponding variables
$\ \cdot\ _F^2$	Frobenius norm: sum of the squared entries of the given variable
\mathcal{S}	the sphere $\{\mathcal{A} : \ \mathcal{A}\ _F = 1\}$
$\psi_\lambda(\mathcal{A}, \mathcal{X})$	objective for fixed λ and given $(\mathcal{A}, \mathcal{X})$
$\varphi_\lambda(\mathcal{A})$	marginalized objective for fixed λ and given \mathcal{A} : $\varphi_\lambda(\mathcal{A}) = \min_{\mathcal{X}} \psi_\lambda(\mathcal{A}, \mathcal{X})$
η	additive Gaussian noise variance
$\text{SNR} \equiv \frac{\text{var}(\mathcal{A})}{\eta}$	signal-to-noise ratio
$\epsilon(\mathcal{A}, \hat{\mathcal{A}})$	error metric: angle between \mathcal{A} and $\hat{\mathcal{A}}$ on the hemisphere
θ	kernel concentration: probability that a pixel of \mathcal{X} is a defect center

I. SIMULATED STM SPECTROSCOPIC MEASUREMENTS ON A SQUARE LATTICE

We consider a two-dimensional structure of atoms forming an infinite periodic square array, with lattice constant a . Under the single-electron Tight-Binding (TB) approximation, electrons are localized to fixed atomic sites [1–3]. This model allows for an inter-site interaction consisting of a hopping integral between nearest-neighboring lattice sites, characterized as the fixed hopping-parameter $t < 0$. The on-site energies of the lattice are assumed to be a constant E_0 . Introducing point defects into the system breaks translational symmetry of the system and perturbs the Local Density of States (LDoS). These point defects are assumed to have an energy of E_j , where j enumerates the number N_d of defects.

We seek to calculate the LDoS $\rho(\vec{x}, \omega)$ for this system with a finite number of point defects. $\rho(\vec{x}, \omega)$ represents the number of states that are available to be occupied by electrons – a measure of the relative probability of finding an electron at location $\vec{x} \in \mathbb{R}^2$ with energy $\omega \in \mathbb{R}$. In STM spectroscopy [4], $\rho(\vec{x}, \omega)$ is recorded as a function of the probe tip location \vec{x} and an applied bias voltage ω between the tip and specimen.

A. Perturbation Theory

The LDoS is determined by the matrix elements of the Green's Function (GF) in the coordinate representation:

$$\rho(\vec{x}, \omega) = \frac{-1}{\pi} \text{Im} \left[\langle \vec{x} | \hat{G} | \vec{x} \rangle \right] \quad (\text{S1})$$

with the GF defined as $\hat{G}(\omega) = (\omega - \hat{H})^{-1}$.

Assuming no direct coupling between the lattice and point defects, the system Hamiltonian \hat{H} can be expressed as the sum of two contributions $\hat{H} = \hat{H}_0 + \hat{H}_1$ where \hat{H}_0 is the TB Hamiltonian for a square lattice and \hat{H}_1 is the impurity Hamiltonian:

$$\hat{H}_1 = \sum_{\alpha=1}^{N_d} E_{\alpha} |\alpha\rangle \langle \alpha|$$

in which α enumerates the N_d point defects, located at distinct positions $\vec{x}_{\alpha} \in \mathbb{R}^2$.

Since \hat{H}_0 can be easily diagonalized in \vec{k} -momentum space, we treat \hat{H}_1 as a perturbation on \hat{H}_0 . In accordance with perturbative scattering theory, the GF can be expressed as:

$$\hat{G} = \hat{G}_0 + \hat{G}_0 \hat{T} \hat{G}_0 \quad (\text{S2})$$

where \hat{G}_0 and \hat{T} are the Bare Lattice Green's Function (BLGF) and the scattering T-matrix, respectively, which satisfy the following:

$$\hat{G}_0(\omega) = \frac{1}{\omega - \hat{H}_0} \quad (\text{S3})$$

$$\hat{T} = \hat{H}_1 \left(\hat{I} - \hat{G}_0 \hat{H}_1 \right)^{-1} \quad (\text{S4})$$

B. Reduction to Matrix Elements

Following the prescription in (S1), we compute the matrix elements of \hat{G} from (S2) to obtain:

$$\rho(\vec{x}, \omega) = \rho^{(0)}(\vec{x}, \omega) + \frac{-1}{\pi} \text{Im} \left[\langle \vec{x} | \hat{G}_0 \hat{T} \hat{G}_0 | \vec{x} \rangle \right]$$

where $\rho^{(0)}(\vec{x}, \omega)$ is the LDoS for a system with no defects. Since experimental probes, such as STM, are sensitive to changes in the LDoS, rather than the LDoS itself, we will treat $\delta\rho(\vec{x}, \omega) \equiv \rho(\vec{x}, \omega) - \rho^{(0)}(\vec{x}, \omega)$ as the physical observable:

$$\delta\rho(\vec{x}, \omega) = \frac{-1}{\pi} \text{Im} \left[\langle \vec{x} | \hat{G}_0 \hat{T} \hat{G}_0 | \vec{x} \rangle \right] = \frac{-1}{\pi} \text{Im} \left[\sum_{\alpha, \beta=1}^{N_d} G_0(\vec{x}, \vec{x}_\alpha) T_{\alpha, \beta} G_0(\vec{x}_\beta, \vec{x}) \right] \quad (\text{S5})$$

with the following defined quantities:

$$G_0(\vec{x}, \vec{y}) = \langle \vec{x} | \hat{G}_0 | \vec{y} \rangle \quad (\text{S6})$$

$$T_{\alpha, \beta} = \langle \alpha | \hat{T} | \beta \rangle \quad (\text{S7})$$

Henceforth, we will refer to $\delta\rho(\vec{x}, \omega)$ in (S5) as the LDoS and vice-versa.

C. Calculation of Matrix Elements

The following section discusses the calculation of matrix elements of \hat{G}_0 and \hat{T} in (S6) and (S7) necessary to determine $\delta\rho(\vec{x}, \omega)$ in (S5).

1. Bare Lattice Green's Function Matrix Elements

We aim to compute the matrix elements of the BLGF in the coordinate representation $G_0(\vec{x}, \vec{x}'; \omega)$. Starting with the definition of the BLGF in (S3), we have:

$$\hat{G}_0 = \int_{\text{BZ}} d\vec{k} \frac{1}{\omega - \hat{H}_0} \left| \vec{k} \right\rangle \left\langle \vec{k} \right| = \int_{\text{BZ}} d\vec{k} \frac{1}{\omega - E_{\vec{k}}} \left| \vec{k} \right\rangle \left\langle \vec{k} \right| \quad (\text{S8})$$

where the integration is across the first Brillouin Zone (BZ). The energy dispersion $E_{\vec{k}}$ of the square lattice is:

$$E_{\vec{k}} = E_0 - 2t (\cos(k_1 a) + \cos(k_2 a)) \quad (\text{S9})$$

Substituting (S9) into (S8) gives the BLGF coordinate representation matrix elements:

$$\begin{aligned} \langle \vec{x} | \hat{G}_0 | \vec{x}' \rangle &= \frac{1}{(2\pi)^2} \int_{\text{BZ}} d\vec{k} e^{i\vec{k} \cdot (\vec{x} - \vec{x}')} \frac{1}{\omega - E_0 - 2t (\cos(k_1 a) + \cos(k_2 a))} \\ G_0(\vec{x}, \vec{x}') &= \frac{1}{(2\pi)^2} \frac{1}{2t} \int_{\text{BZ}} d\vec{k} \frac{e^{ik_1(x_1 - x'_1)} e^{ik_2(x_2 - x'_2)}}{b - (\cos(k_1 a) + \cos(k_2 a))} \end{aligned} \quad (\text{S10})$$

where $b \equiv \frac{\omega - E_0}{2t}$ is a dimensionless parameter with a complex $\omega \rightarrow \omega + i\epsilon$ analytic continuation. Defining the normalized position deviations as $s_j \equiv \frac{1}{a}(x_j - x'_j)$, (S10) can be reduced to quadratures:

$$\begin{aligned}
G_0(\vec{x}, \vec{x}') &= \frac{1}{(2\pi)^2} \frac{1}{2t} \int_{-\frac{\pi}{a}}^{\frac{\pi}{a}} \int_{-\frac{\pi}{a}}^{\frac{\pi}{a}} \frac{dk_1 dk_2 e^{ik_1 a s_1} e^{ik_2 a s_2}}{b - (\cos(k_1 a) + \cos(k_2 a))} \\
G_0(\vec{x}, \vec{x}') &= \frac{1}{(2\pi)^2} \frac{1}{2t} \frac{4}{a^2} \int_0^\pi \int_0^\pi d\phi_1 d\phi_2 \frac{\cos(\phi_1 s_1) \cos(\phi_2 s_2)}{b - \cos \phi_1 - \cos \phi_2} \\
G_0(\vec{x}, \vec{x}') &= \frac{1}{(2\pi)^2} \frac{1}{2t} \frac{4}{a^2} I_{\text{sq}} \left(\frac{x_1 - x'_1}{a}, \frac{x_2 - x'_2}{a}, b \right)
\end{aligned} \tag{S11}$$

where we define the 2-dimensional definite integral I_{sq} as:

$$I_{\text{sq}}(s_1, s_2, b) \equiv \int_0^\pi \int_0^\pi d\phi_1 d\phi_2 \frac{\cos(s_1 \phi_1) \cos(s_2 \phi_2)}{b - \cos \phi_1 - \cos \phi_2} \tag{S12}$$

2. Scattering T-Matrix Elements

We are also interested in computing the matrix elements of \hat{T} between defects, as described in (S7). Recalling that E_α is the on-site energy of the defect located at \vec{x}_α , the defect-defect matrix elements of (S4) are:

$$\begin{aligned}
T_{\alpha, \beta} &= \langle \alpha | \hat{H}_1 \left(\hat{I} - \hat{G}_0 \hat{H}_1 \right)^{-1} | \beta \rangle \\
&= E_\alpha \langle \alpha | \left(\hat{I} - \hat{G}_0 \hat{H}_1 \right)^{-1} | \beta \rangle \\
T_{\alpha, \beta} &= E_\alpha (\delta_{\alpha, \beta} - E_\beta G_0(\vec{x}_\alpha, \vec{x}_\beta))^{-1}
\end{aligned} \tag{S13}$$

The scattering T-matrix elements are completely determined by (S13) once the BLGF matrix elements are obtained in (S11).

D. Numerical Results on a Single Point Impurity

Embedded within the $T_{\alpha, \beta}$ calculation in (S13) is a matrix inverse involving the matrix elements of \hat{G}_0 corresponding to inter-defect scatterings. However if we consider the $N_d = 1$ single impurity limit, we can bypass the formal matrix inversion. In this limit, the scattering T-matrix becomes a scalar

$$T(\omega) = \frac{1}{E_1^{-1} - G_0(\vec{x}_d, \vec{x}_d; \omega)} \tag{S14}$$

where the impurity location is $\vec{x}_d \in \mathbb{R}^2$. Substituting (S14) into (S5) gives $\delta\rho(\vec{x}, \omega)$ in the presence of a single point impurity:

$$\begin{aligned}\delta\rho(\vec{x}, \omega) &= \frac{-1}{\pi} \operatorname{Im} \left[\frac{G_0(\vec{x}, \vec{x}_d; \omega) G_0(\vec{x}_d, \vec{x}; \omega)}{E_1^{-1} - G_0(\vec{x}_d, \vec{x}_d; \omega)} \right] \\ \delta\rho(\vec{x}, \omega) &= \frac{-1}{\pi} \operatorname{Im} \left[\frac{G_0^2(\vec{x}, \vec{x}_d; \omega)}{E_1^{-1} - G_0(\vec{x}_d, \vec{x}_d; \omega)} \right]\end{aligned}\quad (\text{S15})$$

To produce simulated single-defect STM measurements to assess the SBD-STM approach, $\delta\rho(\vec{x}, \omega)$ was computed at all measurement positions \vec{x} for a particular fixed value of defect energy E_d , hopping parameter t , measurement energy ω , and specified defect location $\vec{x}_d = \vec{0}$. Conforming with typical STM experimental datasets, the measurement grid consisted of 256×256 equally-spaced points chosen to overlap with the square lattice containing N^2 atomic sites, with $N = 50$. $\delta\rho(\vec{x}, \omega)$ was numerically computed at every grid point at 41 different energy ω values. Typical LDoS maps of single-defect square lattice systems are shown in Supplementary Figure S-I.

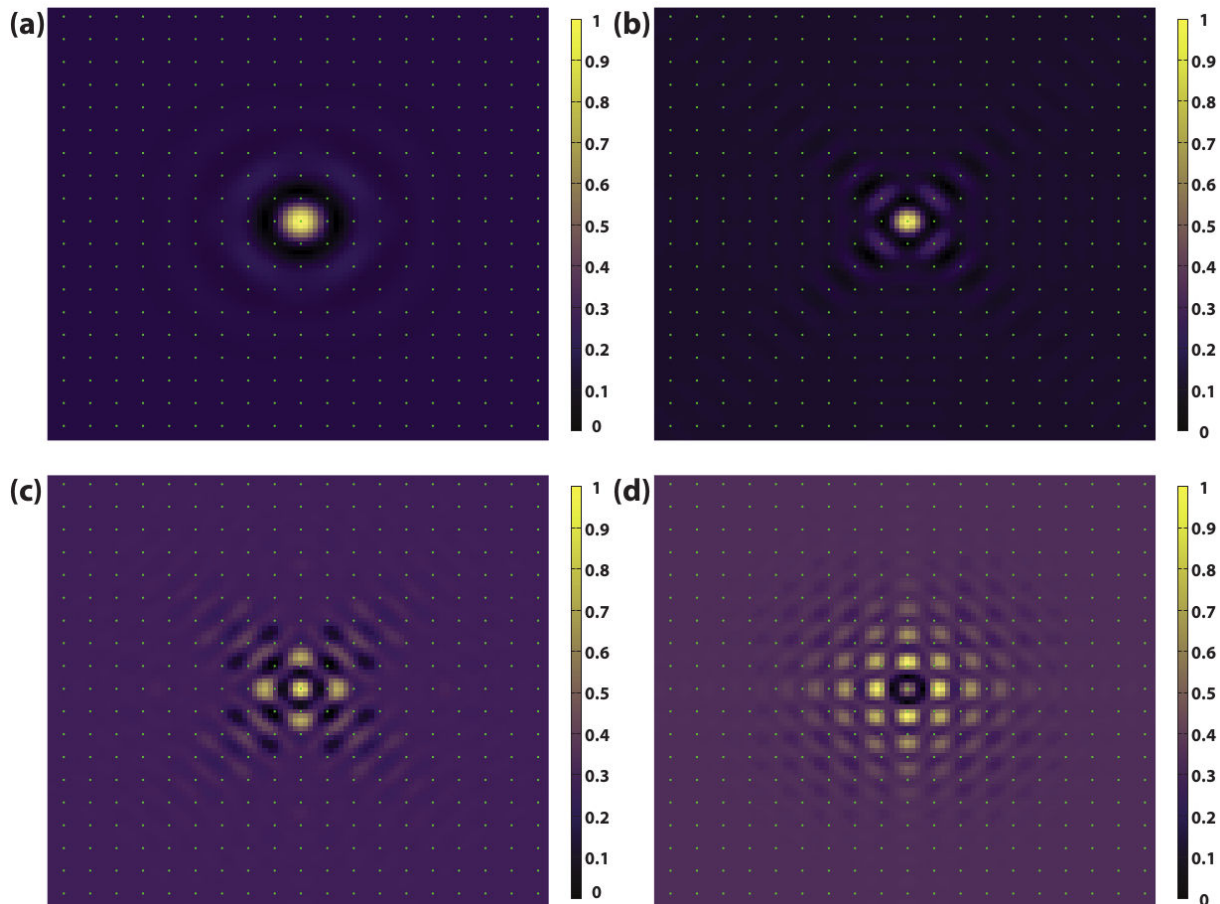
One observes that the LDoS resulting from a single impurity has a structure entangled with the underlying atomic lattice. As the probe energy ω changes, the LDoS signatures also modulate in the vicinity of the defect. Far away from the defect ($\gtrsim 10$ atomic lengths), $\delta\rho(\vec{x}, \omega)$ is nearly constant.

E. Numerical Results on Multiple Point Defects

Simulations on square lattice systems possessing multiple point defects have also been implemented using (S5). Shown in Supplementary Figure S-II are representative calculated LDoS maps at different energies for 70 point impurities randomly distributed on the square lattice. As expected, the effect of multiple defect scattering is more vivid at locations where the defects are clustered together.

II. SPARSE INVERSE PROBLEMS

The convolutional model proposed in equation (1) of the main text provides a concise description of STM datasets. However, the problem of inferring \mathcal{A}_0 and \mathcal{X}_0 from \mathcal{Y} alone is ill-posed in general – for $s \in \mathbb{N}$ voltage slices, one must extract $n_1 n_2 + s \cdot m_1 m_2$ values from $s \cdot n_1 n_2$ observed pixels. Even with many voltage slices, our kernel slices from \mathcal{A}_0 are

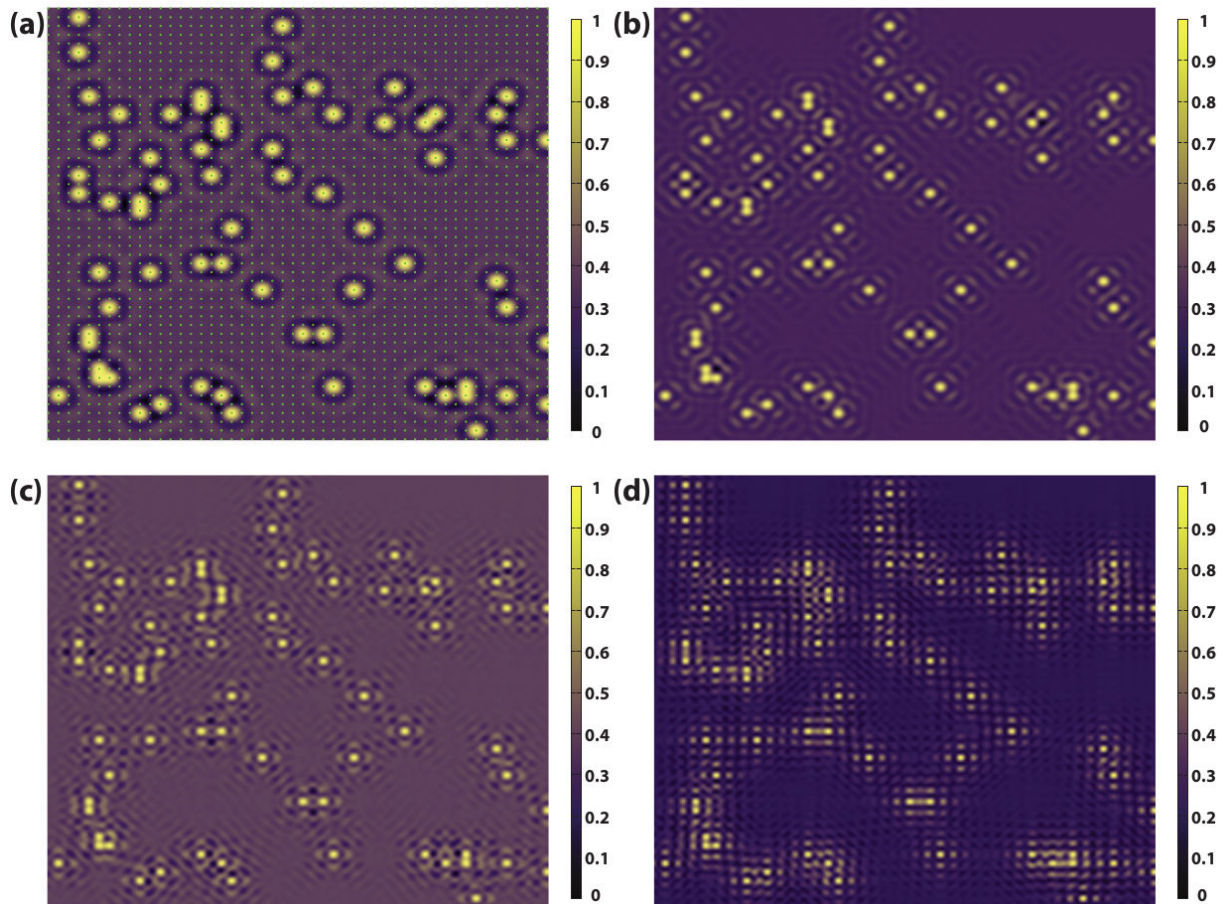


Supplementary Figure S-I. $\delta\rho(\vec{x},\omega)$ for a single impurity on a square lattice with $t = -0.2$ and $\omega = -0.5$ (a), 0 (b), $+0.2$ (c), and $+0.35$ (d). All LDoS maps are normalized between 0 and 1. The arrays of green dots are guides to the eyes indicating the atomic positions of the square lattice.

approximately low-pass and vary slowly across bias voltages, so the problem of recovering \mathcal{X}_0 would remain ill-posed even if \mathcal{A}_0 were known a priori. Since our problem involves inferring both \mathcal{A}_0 and \mathcal{X}_0 , it is essential to incorporate well-motivated assumptions about the structure of the data.

In this work, we capitalize on the *sparsity* of \mathcal{X}_0 to render the problem well-posed. Informally, \mathcal{X}_0 is sparse if most of its entries are zero. The sparse signal model is applicable whenever one is interested in signals that are composed of a few components from a large “dictionary”: although one can find defects at any location in \mathcal{X}_0 within the convolutional model, the expected number of defects in typical STM datasets is much smaller than the number of pixels in the image.

The power of sparsity is most clearly illustrated within the context of *linear inverse problems*. For instance, suppose one is given a matrix $\mathbf{D} \in \mathbb{R}^{m \times n}$ and an observation



Supplementary Figure S-II. $\delta\rho(\vec{x}, \omega)$ for 70 impurities randomly distributed on a 50×50 atom square lattice with $t = -0.2$ and $\omega = -0.5$ (a), 0 (b), $+0.2$ (c), and $+0.35$ (d). All LDoS maps are normalized between 0 and 1. The array of green dots in (a) is a guide to the eyes indicating the atomic positions of the square lattice. Point defects are located at the same atomic positions.

$\mathbf{y} = \mathbf{D}\mathbf{x}_0$, and wishes to recover \mathbf{x}_0 . When $m \ll n$, this is an ill-posed problem with infinitely many solutions. However, if \mathbf{x}_0 is known to be sparse, we can attempt to recover \mathbf{x}_0 by solving the following optimization problem, which seeks the *sparsest* solution to the underdetermined linear system $\mathbf{y} = \mathbf{D}\mathbf{x}$:

$$\begin{cases} \underset{\mathbf{x}}{\text{minimize}} & \|\mathbf{x}\|_0 \\ \text{subject to} & \mathbf{D}\mathbf{x} = \mathbf{y}. \end{cases} \quad (\text{S16})$$

Here the ℓ_0 -“norm” $\|\mathbf{x}\|_0$ counts the number of nonzero entries in the vector \mathbf{x} . Under very general conditions, the unique optimal solution to (S16) is \mathbf{x}_0 , the signal that generated the observation \mathbf{y} . For example, for a generic choice of \mathbf{D} , \mathbf{x}_0 is the unique optimal solution to (S16), provided it has nonzero entries, k , that are less than half the number of observations

$m > 2k$. In this situation, imposing sparsity constraints renders an ostensibly ill-posed inverse problem well-posed [5].

The optimization in (S16) is purely conceptual in nature: it involves a search over all possible sets of nonzero entries for the vector \mathbf{x} , and hence is intractable even for small m and n . To address this issue, many computationally efficient heuristics have been developed as alternatives to ℓ_0 -norm minimization for computing sparse solutions. One popular heuristic is to *relax* (S16) by replacing the ℓ_0 -norm $\|\mathbf{x}\|_0$ with the ℓ_1 -norm $\|\mathbf{x}\|_1 = \sum_{i=1}^n |x_i|$, leading to a convex optimization problem known as *basis pursuit*:

$$\begin{cases} \underset{\mathbf{x}}{\text{minimize}} & \|\mathbf{x}\|_1 \\ \text{subject to} & \mathbf{D}\mathbf{x} = \mathbf{y}. \end{cases} \quad (\text{S17})$$

This problem can be converted to a linear program, and hence solved in polynomial time using general-purpose tools. A variety of dedicated algorithms are also available for (S17), which can efficiently solve very large instances to an accuracy acceptable for modern statistical and signal processing applications. In short, replacing the ℓ_0 -norm with the ℓ_1 -norm yields a problem that we can efficiently solve, at scale, on contemporary hardware.

However, a crucial question arises: *have we lost anything in moving from the problem that we would like to solve (ℓ_0 minimization) to a problem that we can solve (ℓ_1 minimization)?* Specifically, does ℓ_1 minimization still recover the sparse signal \mathbf{x}_0 ? The answer to the second question is a qualified “yes.” Perhaps surprisingly, tractable ℓ_1 minimizations also exactly recover \mathbf{x}_0 , provided that (i) \mathbf{D} is sufficiently “nice,” and (ii) \mathbf{x}_0 is sufficiently sparse. For example, for generic (random) \mathbf{D} , if \mathbf{x}_0 has at most k nonzero entries, basis pursuit succeeds when

$$m \geq C \cdot k \cdot \log(n/k), \quad (\text{S18})$$

in which C is a fixed constant [6, 7]. If we consider m as the number of measurements we have observed, this recovery rate is nearly optimal: \mathbf{x}_0 has k nonzero entries, and it can be efficiently recovered from about $k \log n$ measurements. These results hold for random \mathbf{D} , but deterministic results are also known – the required property, coarsely stated, is that sparse vectors \mathbf{x} cannot be too close to the nullspace of \mathbf{D} . This requirement makes intuitive sense: any sparse vector \mathbf{x} that produces a measurement very close to zero ($\mathbf{y} = \mathbf{D}\mathbf{x} \simeq \mathbf{0}$) will become very difficult to recover, especially in the presence of noise.

If measurements are contaminated with zero-mean additive noise, i.e. $\mathbf{y} = \mathbf{D}\mathbf{x}_0 + \mathbf{w}$, then a popular choice for estimating \mathbf{x}_0 involves solving the LASSO problem [8],

$$\min_{\mathbf{x}} \underbrace{\frac{1}{2} \|\mathbf{D}\mathbf{x} - \mathbf{y}\|_2^2}_{\text{data fidelity}} + \lambda \underbrace{\|\mathbf{x}\|_1}_{\text{sparsity}}. \quad (\text{S19})$$

This formulation balances between a standard least squares term, which ensures fidelity to the observed data, and an ℓ_1 -norm *regularizer*, which biases \mathbf{x} towards sparse solutions. When \mathbf{D} is randomly chosen, Ref. 9 asserts that – with similar sampling requirements to (S18) – solving (S19) will recover the correct sign pattern from \mathbf{x}_0 , provided that λ and the entries of \mathbf{x}_0 are large enough to overcome the bias introduced by the regularizer $\|\mathbf{x}\|_1$ and the variance of the noise term.

Theoretical guarantees of this nature inform the algorithmic design for applications in science and engineering under a variety of settings; we refer the interested reader to Refs. 10 and 11 and the text Ref. 12. For example, in biomedical imaging, these efforts help establish performance and resource requirements in systems where minimal imaging time or radiation dosage are of critical importance [13].

A. The Sparse Convolutional Model for the STM datasets

In this section, we show how to express the STM model, presented in equation (1) of the main text, as a convolution between a defect signature and a sparse activation map, and describe how to estimate the sparse activation map using the LASSO (S19). In this formulation, \mathbf{D} plays the role of the convolution with the defect signature, and \mathbf{x} represents the sparse activation map. Previously, \mathbf{D} was assumed to be known beforehand, but in STM data analysis, we must simultaneously estimate \mathbf{D} and \mathbf{x} . In the next section, we will describe the technical challenges associated with this harder problem, and offer an efficient algorithm that accurately estimates both \mathbf{D} and \mathbf{x} , on well-structured numerical examples.

Restricting the STM image and the defect locations \vec{x}_j to an infinitely large grid of pixel locations \mathbb{Z}^2 and using γ to denote the Kronecker delta so that $\gamma(\vec{u}) = 1$ if $\vec{u} = \vec{0}$ and $\gamma(\vec{u}) = 0$ elsewhere, we have:

$$\delta\rho(\vec{x}, \omega) = \sum_{j=1}^N c_j \cdot \delta\rho_0(\vec{x} - \vec{x}_j, \omega) = \sum_{\vec{u} \in \mathbb{Z}^2} \delta\rho_0(\vec{x} - \vec{u}, \omega) \cdot \underbrace{\left(\sum_{j=1}^N c_j \cdot \gamma(\vec{u} - \vec{x}_j) \right)}_{\text{collect spikes}}.$$

Collecting the defect locations into $\Gamma(\vec{x}) \equiv \sum_{j=1}^N c_j \gamma(\vec{x} - \vec{x}_j)$ leads to the *convolution sum* [14] between $\delta\rho_0$ and Γ ,

$$\delta\rho(\vec{x}, \omega) = \sum_{\vec{u} \in \mathbb{Z}^2} \delta\rho_0(\vec{x} - \vec{u}, \omega) \cdot \Gamma(\vec{u}) = (\delta\rho_0 * \Gamma)(\vec{x}, \omega). \quad (\text{S20})$$

Naturally, mild assumptions are needed on the sizes of the observation $\delta\rho$, defect locations \vec{x}_j , and LDoS signature $\delta\rho_0$. Letting $W_n = \{0, \dots, n_1 - 1\} \times \{0, \dots, n_2 - 1\}$ be the observation window, we assume that $\delta\rho(\vec{x}, \omega) = 0$ for any $\vec{x} \notin W_n$, and $\bigcup_j \vec{x}_j \subseteq W_n$, i.e. the observations and defect locations are bounded within an $n_1 \times n_2$ window. We also assume that $m_1 \ll n_1$, and $m_2 \ll n_2$ so that the individual defect signature takes up a relatively small portion of the observation window W_m .

Denoting the discretized versions of the activation map, the LDoS signature of a single impurity, and the full STM image – with energies discretized to s levels – by $\mathcal{X}_0 \in \mathbb{R}^{n_1 \times n_2}$, $\mathcal{A}_0 \in \mathbb{R}^{n_1 \times n_2 \times s}$, and $\mathcal{Y} \in \mathbb{R}^{m_1 \times m_2 \times s}$ respectively, we have

$$\mathcal{Y}(\cdot, \omega) = \mathcal{A}_0(\cdot, \omega) * \mathcal{X}_0,$$

which we express concisely as $\mathcal{Y} = \mathcal{A}_0 \boxtimes \mathcal{X}_0$. \mathcal{X}_0 is expected to be sparse in this formulation, otherwise the observation would be saturated with defects. Since the convolution operator \boxtimes is linear with respect to each argument, a LASSO problem can be solved to produce a sparse estimate of \mathcal{X}_0 from a noisy observation, provided that \mathcal{A}_0 is known:

$$\hat{\mathcal{X}} \leftarrow \min_{\mathcal{X}} \frac{1}{2} \|\mathcal{A}_0 \boxtimes \mathcal{X} - \mathcal{Y}\|_F^2 + \lambda \|\mathcal{X}\|_1 \quad (\text{S21})$$

This is an example of a *Sparse Deconvolution* (SD) problem. (Recall that the *Frobenius norm* $\|\cdot\|_F^2$ is the sum of square entries in the tensorial setting.)

On the contrary, \mathcal{A}_0 is unknown in the STM setting, leading to a bilinear inverse problem known as *Blind Deconvolution* (BD). However, assuming that a good approximation of the observation \mathcal{Y} can only be produced by convolving a sparse activation map \mathcal{X} with a candidate kernel \mathcal{A} once $\mathcal{A} \simeq \mathcal{A}_0$, the optimal objective value from (S21) may serve as a basis for finding \mathcal{A} by formulating the problem

$$(\hat{\mathcal{A}}, \hat{\mathcal{X}}) \leftarrow \min_{\mathcal{A}} \min_{\mathcal{X}} \frac{1}{2} \|\mathcal{A} \boxtimes \mathcal{X} - \mathcal{Y}\|_F^2 + \lambda \|\mathcal{X}\|_1 \quad (\text{S22})$$

as an instance of the *Sparse Blind Deconvolution* (SBD) problem. This problem is nonconvex, and consequently, characterizing the performance of efficient algorithms is challenging:

currently available theory does not completely explain the good behavior of simple nonconvex methods on practical problems. Nevertheless, this problem is part of a rapidly developing area of study with practical and theoretical implications.

B. Relevant problems and literature

Recently, variants of the deconvolution and BD problems have attracted significant theoretical interest. For instance, Refs. 15–17 study the solvability of BD problems under various settings. However strong assumptions are often needed, and the settings studied thus far do not staunchly align with our SBD setting (S22).

While the difficulty of establishing theory for nonconvex optimization makes guarantees for SBD problem difficult to formulate, many of the same concerns in existing literature motivate our SBD-STM algorithm and its analysis: the effect of various sparsity levels, noise power, and the choice of tradeoff parameter λ are motivated by studies involving the LASSO problem (S19).

Studies involving variants of the SD problem are more extensive, and provide an important source of intuition for the SBD problem. For example, Ref. 18 suggests that even when \mathcal{A}_0 is known in advance, the recoverability of the *activation locations* depends strongly on the distance between these locations in \mathcal{X}_0 as well as the conditioning of \mathcal{A}_0 and the noise level. As a result, it is difficult to expect perfect recovery of the defect locations from $\hat{\mathcal{X}}$, especially when the kernels in \mathcal{A}_0 are approximately low-pass and under copious noise.

Practically, deconvolution problems are of interest in a large variety of fields. The extraction of spike signals in neuroscience [19] and the deblurring of images [20] serve as quintessential examples of problems that rely critically on a (blind) deconvolutional model. We refer interested readers to Refs. 21 and 22 for more details.

III. SOLVING THE SBD-STM PROBLEM

A. Symmetries and Nonconvexity

The bilinearity of the convolutional model $\mathcal{Y} = \mathcal{A}_0 \boxtimes \mathcal{X}_0$ leads to a number of difficulties characterizing or solving the problem (S22). One class of difficulties arises due to symmetry, in the sense that there are many distinct choices of $(\mathcal{A}, \mathcal{X})$ that are equally sparse *and*

approximate \mathcal{Y} equally well. Having to work with entire equivalence classes of $(\mathcal{A}, \mathcal{X})$ introduces computational issues and makes characterizing our solution quality of the SBD-STM problem difficult, so modifications for breaking such symmetries are needed. The methods used to resolve undesirable phenomena arising from such symmetries lead to many sources of nonconvexity that require special consideration for yielding robust and reliable estimates of \mathcal{A}_0 and \mathcal{X}_0 .

1. Optimization on the sphere

One consequence of bilinearity is *scaling symmetry*: for any \mathcal{A} , \mathcal{X} , and scalar $\alpha \in \mathbb{R}$ scaling one variable up and the other down by α leads to the same convolution, i.e. $\mathcal{A} \boxtimes \mathcal{X} = (\alpha\mathcal{A}) \boxtimes (\alpha^{-1}\mathcal{X})$. Because the ℓ_1 -norm is a relaxation of the ℓ_0 -norm and not a true sparsity measure, solutions that essentially have the same data fidelity and sparsity can lead to wildly different objective values through rescaling by α . This undesirable trait is addressed by fixing \mathcal{A} to lie on the sphere $\mathcal{S} = \{\mathcal{A} \in \mathbb{R}^{m_1 \times m_2 \times s} : \|\mathcal{A}\|_F = 1\}$, which greatly restricts the equivalence class due to scaling symmetry to that of sign flips $\mathcal{A} \boxtimes \mathcal{X} = (-\mathcal{A}) \boxtimes (-\mathcal{X})$. However, the optimization problem must now be solved over a nonconvex manifold \mathcal{S} , requiring modifications to standard optimization tools so that operations applied to produce updates are consistent with the geometry of \mathcal{S} .

2. Shifting symmetry produces local minima

The convolution sum contains a *shifting symmetry* when operating on functions over \mathbb{Z}^2 : shifting the activation map and the LDoS signature by $\vec{\Delta} = (\Delta_1, \Delta_2)$ pixels in opposite directions yields the same observation. From (S20), observe that

$$\begin{aligned} \delta\rho(\vec{x}, \omega) &= (\delta\rho_0 * \Gamma)(\vec{x}, \omega) \\ &= \sum_{\vec{u} \in \mathbb{Z}^2} \delta\rho_0(\vec{x} - \vec{u}, \omega) \cdot \Gamma(\vec{u}) \\ &= \sum_{\vec{u} \in \mathbb{Z}^2} \delta\rho_0\left((\vec{x} - \vec{u}) + \vec{\Delta}, \omega\right) \cdot \Gamma\left(\vec{u} - \vec{\Delta}\right) \\ \delta\rho(\vec{x}, \omega) &= \mathcal{T}\left[\delta\rho_0; \vec{\Delta}\right](\vec{x}, \omega) * \mathcal{T}\left[\Gamma; -\vec{\Delta}\right](\vec{x}, \omega) \end{aligned}$$

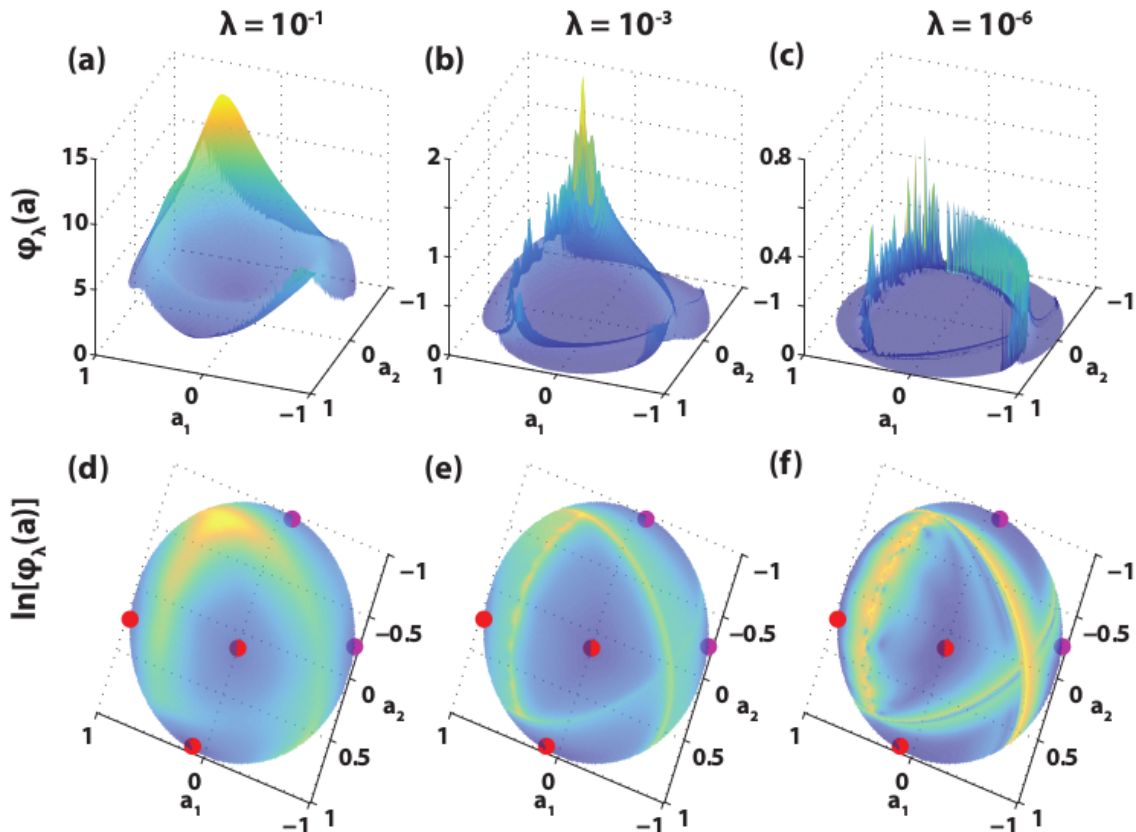
where the shift-translation operator \mathcal{T} of a function $f(\vec{x})$ is defined as: $\mathcal{T} [f; \vec{\Delta}] (\vec{x}) \equiv f(\vec{x} + \vec{\Delta})$.

The restriction of $\delta\rho$ to the size of \mathcal{A} breaks this symmetry, since the shift $(\mathcal{T} [\mathcal{A}_0; \vec{\Delta}], \mathcal{T} [\mathcal{X}_0; -\vec{\Delta}])$ from $(\mathcal{A}_0, \mathcal{X}_0)$ would yield worse data fidelity if any signal from $\delta\rho$ were shifted outside the size of \mathcal{A} . On the other hand, this restriction condition is very weak: the loss in data fidelity can be insignificant when the window sizes are large. Indeed, such *shift-truncations* are often achieved by methods employed to solve problems similar to (S22) – we discuss attempts to refine solutions from shift-truncations further in Section III B 2.

As a result of the sign and shifting symmetries, objectives related to (S22) possess several local minima in the form of *signed shift-truncations*, making the objective function nonconvex as demonstrated in Supplementary Figure S-III. In general, nonconvex problems are notorious for local minima or undesired critical points that are difficult to anticipate and characterize. Indeed, visualizations (see Supplementary Figure S-III) of the objective in low-dimensional cases confirm that the objective is geodesically nonconvex in general, containing several saddle points and local minima.

In such situations, finding a method that can reliably reach local minima becomes more involved. For the present study we employ the Riemannian Trust-Region Method (RTRM) [23]. The standard TRM produces updates for iterates in Euclidean space by minimizing a quadratic approximation of the objective within a neighborhood of the iterate. The neighborhood radius is maintained at each iteration to limit the deviation of the quadratic approximation from the true objective. This procedure results in a second-order method guaranteeing that a local minimum will be attained so long as the stationary points of the objective are nondegenerate. The RTRM extends this method to Riemannian submanifolds embedded in Euclidean spaces – such as the sphere \mathcal{S} – by augmenting TRM operations to become consistent with the manifold geometry. Consequently, the RTRM provides strong guarantees that a local minimum of the objective will be attained over \mathcal{S} .

Other descent methods can potentially be extended to find local minima in a manifold setting. Except for pathological examples, solving problems on Euclidean spaces using gradient descent with random initializations will converge to a local minimum almost surely [24], and noisy gradient descent is guaranteed to efficiently converge to a local minimum [25]. As a second-order method, TRM enjoys significantly faster convergence with regards to iterations but with increased computation per iteration, as well as better overall tail convergence



Supplementary Figure S-III. Objective function geometry with varying values of λ . (a)-(c) The objective $\varphi_\lambda(\mathbf{a}) = \min_{\mathbf{x}} \frac{1}{2} \|\mathbf{a} * \mathbf{x} - \mathbf{a}_0 * \mathbf{x}_0\|_2^2 + \lambda \|\mathbf{x}\|_1$ over the hemisphere $\{(a_1, a_2) : a_1^2 + a_2^2 \leq 1\}$ for $\lambda = 10^{-1}$, 10^{-3} , and 10^{-6} . Each pair (a_1, a_2) uniquely determines $\mathbf{a} \in \mathbb{S}^2$. The truth kernel is $\mathbf{a}_0 = \mathbb{P}_{\mathbb{S}^2}([1, 8, 2])$ (the vector $[1, 8, 2]$ projected onto the sphere) and entries of $\mathbf{x}_0 \in \mathbb{R}^{256}$ are drawn independently and randomly from a Bernoulli-Gaussian distribution with $x_i \stackrel{\text{i.i.d.}}{\sim} \text{Bern}(0.1) \cdot \mathcal{N}(0, 1)$. (d)-(f) Logarithm of the objective functions shown in (a)-(c), respectively. The truth kernel \mathbf{a}_0 and its shift-truncations $\mathbb{P}_{\mathbb{S}^2}([8, 2, 0])$, $\mathbb{P}_{\mathbb{S}^2}([0, 1, 8])$ are shown in red, and sign-flips $\mathbb{P}_{\mathbb{S}^2}(-[8, 2, 0])$, $\mathbb{P}_{\mathbb{S}^2}(-[0, 1, 8])$ are shown in magenta. Brighter colors on the surface plots indicate higher objective value. Notice that each signed shift-truncation shown on the hemisphere is close to a corresponding local minimum. Furthermore, the objective landscape becomes less regularized as λ shrinks, with many local minima appearing for $\lambda = 10^{-6}$.

(when iterates are close to local minima).

B. Solving the SBD-STM Problem with RTRM

1. Smoothing the Sparse Regularizer

Although we would like to solve problem (S22) using RTRM, the presence of the ℓ_1 regularizer forbids second-order information to be extracted from $\varphi_\lambda(\mathcal{A}) = \min_{\mathcal{X}} \psi_\lambda(\mathcal{X}, \mathcal{A}) = \min_{\mathcal{X}} \frac{1}{2} \|\mathcal{A} \boxtimes \mathcal{X} - \mathcal{Y}\|_F^2 + \lambda \cdot r(\mathcal{X})$. Since the variable \mathcal{X} is marginalized by solving the convex problem

$$\mathcal{X}_*(\mathcal{A}; \lambda) \leftarrow \min_{\mathcal{X}} \frac{1}{2} \|\mathcal{A} \boxtimes \mathcal{X} - \mathcal{Y}\|_F^2 + \lambda \cdot r(\mathcal{X}) \quad (\text{S23})$$

dependent on \mathcal{A} , computing the Hessian $\nabla_{\mathcal{A}, \mathcal{A}}^2 \varphi_\lambda(\mathcal{A})$ requires access to $\nabla_{\mathcal{X}, \mathcal{X}}^2 \psi_\lambda(\mathcal{A}, \mathcal{X})$, which does not exist when ℓ_1 -norm is present. Instead, a regularizer that enjoys the existence of second derivatives should be chosen to approximate the ℓ_1 -norm. For this problem, we choose the *pseudo-Huber* regularizer $r_\mu(\mathcal{X})$, so that:

$$r(\mathcal{X}) = r_\mu(\mathcal{X}) \equiv \sum_{i,j} \mu^2 \left(\sqrt{1 + \mu^{-2} \cdot \mathcal{X}_{i,j}^2} - 1 \right), \quad (\text{S24})$$

where μ would typically be a small positive scalar ($\mu = 10^{-6}$ is chosen in experiments). We see that although $\lim_{\mu \rightarrow 0} r(\cdot) = \|\cdot\|_1$, this function has continuous derivatives of all orders.

Using a smoothed regularizer also helps to avoid troublesome high-order critical points. Although the ℓ_1 -norm is a popular regularizer for producing sparse solutions, it can be problematic in the context of bilinear inverse problems. When \mathcal{A} is far from $\pm \mathcal{A}_0$ on the sphere, solving $\mathcal{X}_* \leftarrow \min_{\mathcal{X}} \frac{1}{2} \|\mathcal{A} \boxtimes \mathcal{X} - \mathcal{Y}\|_2^2 + \lambda \|\mathcal{X}\|_1$ encourages entries of \mathcal{X} to be exactly zero. If the entire coefficient map \mathcal{X} is zero, then the gradient of φ with respect to \mathcal{A} is also zero, and descent methods make no progress. Employing a regularizer that encourages a few elements of \mathcal{X}_* to be large, while keeping other elements small (or “approximately sparse”) circumvents this problem as the gradient is unlikely vanish.

Modified minimization problem. Based on the discussion above, we solve the following problem rather than (S22):

$$(\hat{\mathcal{A}}, \hat{\mathcal{X}}) \leftarrow \min_{\mathcal{A} \in \mathcal{S}} \left\{ \varphi_\lambda(\mathcal{A}) \equiv \min_{\mathcal{X}} \left[\psi_\lambda(\mathcal{A}, \mathcal{X}) \equiv \frac{1}{2} \|\mathcal{A} \boxtimes \mathcal{X} - \mathcal{Y}\|_F^2 + \lambda \cdot r(\mathcal{X}) \right] \right\} \quad (\text{S25})$$

which is the objective discussed in equation (4) of the main text.

2. Implementation of RTRM

The MATLAB package ManOpt [26] is used solve (S25) using RTRM. To produce a quadratic approximation of the objective, one needs the ability to compute $\varphi_\lambda(\mathcal{A})$, $\nabla_{\mathcal{A}}\varphi_\lambda(\mathcal{A})$ as well as $\nabla_{\mathcal{A},\mathcal{A}}^2\varphi_\lambda(\mathcal{A})$ for any $\mathcal{A} \in \mathcal{S}$. By rewriting the convolution operator \boxtimes in terms of *cyclic convolutions*, compact expressions can be derived for both the (Euclidean) gradient and Hessian, which are then mapped to their Riemannian equivalents via tools from the package. As an additional benefit, expression in terms of cyclic convolutions allows fast computation of \boxtimes via the FFT.

As discussed earlier, the ℓ_1 regularizer is replaced with the pseudo-Huber norm to make second-order information available to the RTRM. The pseudo-Huber regularizer allows the precise solution of (S23) to be found using the algorithm proposed by Fountoulakis and Gondzio [27], which reports good performance when the observations are generated from a poorly conditioned linear system. Since the individual voltage slices of \mathcal{A} are expected to be smooth and low-pass in the Fourier domain, the case where $(\mathcal{A} \boxtimes \cdot)$ is poorly conditioned is of practical interest.

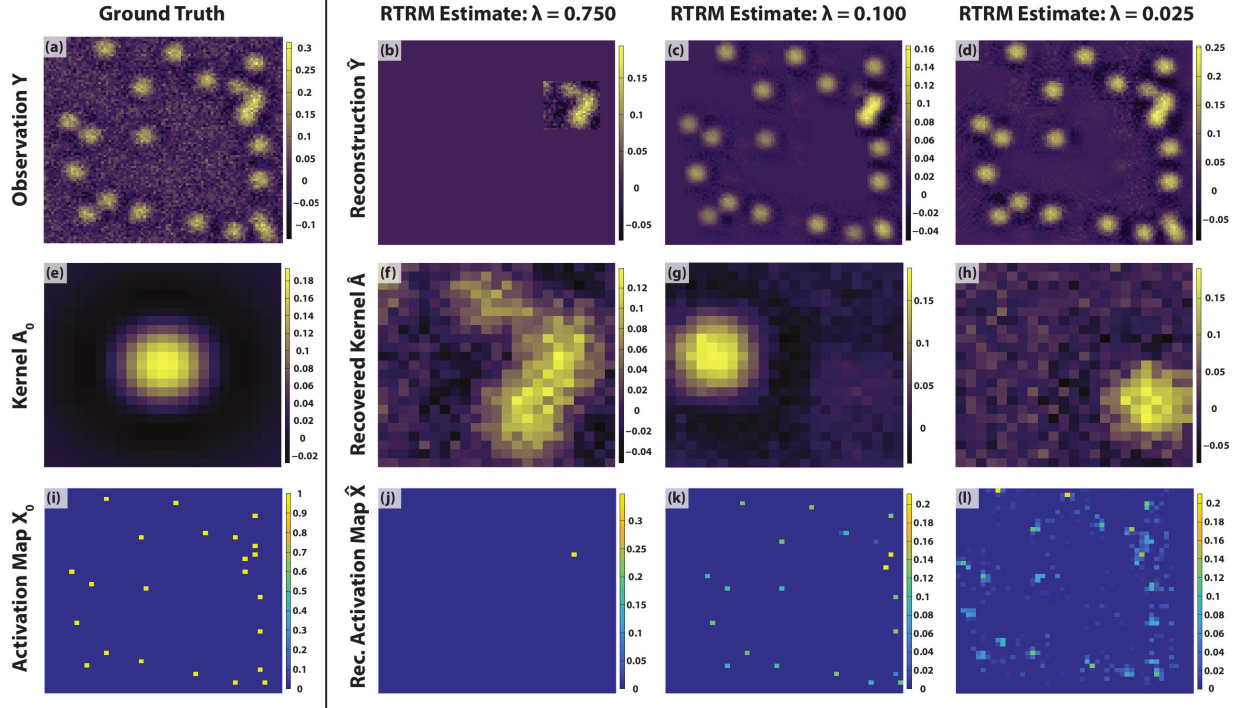
The availability of a method to compute φ_λ and its Riemannian gradient and Hessian allows one to solve (S25) using RTRM. We denote this procedure using the notation

$$\hat{\mathcal{A}} \leftarrow \text{ASolve}(\mathcal{A}_{\text{init}}, \lambda; \mathcal{Y}, (m_1, m_2)),$$

passing the regularization parameter λ and an initialization $\mathcal{A}_{\text{init}}$ for \mathcal{A} as input arguments. The dependence of **ASolve** on the observation \mathcal{Y} and the kernel size (m_1, m_2) (which is implicitly provided by $\mathcal{A}_{\text{init}}$) is explicitly made, although we will write **ASolve** $(\mathcal{A}_{\text{init}}, \lambda)$ for brevity when the observation and kernel sizes are clear by context.

Poor estimates of $\hat{\mathcal{A}}$ can occur due to overfitting the noise term in the observation \mathcal{Y} . Higher values of λ help retain the quality of $\hat{\mathcal{A}}$ by enforcing sparsity in $\hat{\mathcal{X}}$. On the other hand, if $\hat{\mathcal{X}}$ becomes too sparse (λ is too large), one can fail to recover activation locations from \mathcal{X}_0 , meaning that there are fewer defects from the \mathcal{Y} being taken into account by **ASolve**. This can also lead to poor estimates of \mathcal{A} .

Empirically, **ASolve** appears to perform well in simulations in which observations are generated by ground truths \mathcal{A}_0 and \mathcal{X}_0 , and the entries of \mathcal{Z} are drawn independently from the Gaussian distribution $\mathcal{N}(0, \eta)$. In particular, if the noise power η is not too high and



Supplementary Figure S-IV. RTRM estimates (without refinement) from a simulated observation $\mathcal{Y} = \mathcal{A} * \mathcal{X} + \mathcal{Z}$, with moderate noise $(\mathcal{Z})_{ij} \sim \mathcal{N}(0, 10^{-3})$ and using selected values of $\lambda = 0.750$, 0.100, and 0.025. The original observation \mathcal{Y} is shown in (a), which was determined through the convolution of the truth kernel \mathcal{A}_0 and truth activation map \mathcal{X}_0 , depicted in (e) and (i), respectively. Reconstructed observations from the convolution $\hat{\mathcal{Y}} = \hat{\mathcal{A}} * \hat{\mathcal{X}}$ for various values of λ are shown in (b)-(d). Observe that recovered kernels (f)-(h) $\hat{\mathcal{A}}$ correspond to shift-truncations of the truth kernel \mathcal{A}_0 shown in (e), but the low-energy side lobes tend to be lost under noise. Recovered activation locations from $\hat{\mathcal{X}}$ in (j)-(l) correspond to shift-truncations of the ground truth \mathcal{X}_0 in (i), but are not exact – recovery is particularly poor for nearby activation locations. Recovery in terms of the locations and relative magnitudes in $\hat{\mathcal{X}}$, as well as the details of $\hat{\mathcal{A}}$, is best when λ is chosen carefully. Setting λ too large causes $\hat{\mathcal{X}}$ to shrink excessively; conversely spurious activation locations are identified when λ is too low. Both situations degrade the quality of the estimate $\hat{\mathcal{A}}$.

\mathcal{X}_0 is sufficiently sparse, then a range of $\lambda \geq 0$ will lead $\hat{\mathcal{A}}$ to approximate *shift-truncations* of \mathcal{A}_0 regardless of the initialization to `ASolve`. This is demonstrated in Supplementary Figure S-IV.

3. The Complete SBD-STM Procedure

To address the issues of overfitting and shift-truncation, the complete SBD-STM procedure (Algorithm 1) refines the initial estimate produced by setting $\lambda = \lambda_0$,

$$\mathcal{A}_*^{(0)} \leftarrow \text{ASolve}(\mathcal{A}_{\text{init}}, \lambda_0),$$

through iterations of `ASolve` over a larger size of \mathcal{A} and a decreasing sequence λ_k of regularization parameters until $\lambda_k \leq \lambda_{\text{end}}$ – this is often referred to as a *graduated optimization* or *continuation* procedure.

Algorithm 1 Complete SBD-STM Procedure

Input:

- Observation $\mathcal{Y} \in \mathbb{R}^{n_1 \times n_2 \times s}$,
- Kernel size (m_1, m_2) ,
- Initial $\lambda_0 \geq 0$, decay rate $\alpha \in [0, 1)$, and final $\lambda_{\text{end}} \geq 0$.

Initial phase:

1. Randomly initialize: $\mathcal{A}^{(0)} \in \mathcal{S} = \mathbb{S}^{m_1 \times m_2 \times s}$.
2. $\mathcal{A}_*^{(0)} \leftarrow \text{ASolve}(\mathcal{A}^{(0)}, \lambda_0)$.

Refinement phase:

1. Lifting: Get $\mathcal{A}^{(1)} \in \mathcal{S}' = \mathbb{S}^{m'_1 \times m'_2 \times s}$ by zero-padding the edges of $\mathcal{A}_*^{(0)}$ with a border of width $\lfloor \frac{m_i}{2} \rfloor$.
2. Set $\lambda_1 = \lambda_0$.
3. Continuation: **Repeat** for $k = 1, 2, \dots$ **until** $\lambda_k \leq \lambda_{\text{end}}$,
 - (a) $\mathcal{A}_*^{(k)} \leftarrow \text{ASolve}(\mathcal{A}^{(k)}, \lambda_k)$,
 - (b) Centering:
 - i. Find the size $m_1 \times m_2$ submatrix of $\mathcal{A}_*^{(k)}$ that maximizes the Frobenius (square) norm across all $m_1 \times m_2$ submatrices.
 - ii. Get $\mathcal{A}^{(k+1)}$ by shifting $\mathcal{A}_*^{(k)}$ so that the chosen $m_1 \times m_2$ restriction is in the center, removing and zeropadding entries as needed.
 - iii. Normalize $\mathcal{A}^{(k+1)}$ so it lies in \mathcal{S}' .
 - (c) Set $\lambda_{k+1} = \alpha \lambda_k$.

Output:

1. Extract $\hat{\mathcal{A}} \in \mathcal{S}$ by extracting the restriction of the final $\mathcal{A}^{(k+1)}$ to the center $m_1 \times m_2$ window.
 2. Find the corresponding activation map $\hat{\mathcal{X}} \in \mathbb{R}^{n_1 \times n_2}$ by solving $\min_{\mathcal{X}} \psi_{\lambda_k}(\hat{\mathcal{A}}, \mathcal{X})$.
-

To deal with shift-truncations, the kernel size is enlarged to $m'_1 \times m'_2$ in the refinement

phase once the initial estimate $\mathcal{A}_*^{(0)}$ is obtained. At the end of each refinement, the variables are shifted so that the $m_1 \times m_2$ submatrix of $\mathcal{A}_*^{(k)}$ with the largest signal energy is centered. The choice of m'_1 and m'_2 depends on how far one expects the $\mathcal{A}_*^{(0)}$ to be shifted from the ground truth \mathcal{A}_0 , but it cannot be too large to prevent the refinements $\mathcal{A}_*^{(k)}$ from converging into a different defect signature far larger than $m_1 \times m_2$ in size. In simulated experiments, we choose $m'_i = m_i + 2 \lfloor \frac{m_i}{2} \rfloor$ for $i = 1, 2$, as it is unlikely a shift-truncation by any more than $\frac{m_i}{2}$ pixels can be a local minimum of φ_{λ_0} .

Regarding graduated continuation, we suggest that λ_0 be chosen relatively large (around 0.1 - 0.5) based our discussion in Section III B 2. This encourages a sparse $\mathcal{X}_*(\mathcal{A}; \lambda)$, and forces the activations to considerably favor regions of the image with prominent defect signatures. Although $\mathcal{A}_*^{(0)}$ will be affected by heavy bias and noise (see Supplementary Figure S-IV), this can be refined in later iterations.

Starting with $\lambda_1 = \lambda_0$, a geometrically decreasing sequence for $\{\lambda_k\}$ is chosen, i.e. $\lambda_k = \alpha \cdot \lambda_{k-1}$ for $k = 2, 3, \dots$. This leaves the user to consider the decay rate $\alpha \in [0, 1)$ and the terminating regularization parameter λ_{end} . Based on Ref. 9, we recommend that λ_{end} be chosen proportionately to $\sqrt{n_1 \cdot n_2 \cdot \eta}$, in which η denotes the additive noise variance. In particular, observe that in the limit as $\lambda \rightarrow 0$ and in the absence of noise, (S25) becomes equivalent to the equally constrained problem

$$\begin{aligned} \min_{\mathcal{X}, \mathcal{A} \in \mathcal{S}} \quad & r(\mathcal{X}) \\ \text{s.t.} \quad & \mathcal{A} \boxtimes \mathcal{X} = \mathcal{Y}. \end{aligned}$$

When considering the decay rate α , a smaller choice of α means fewer refinements are needed. However, we would also like to decrease slowly enough so that $\varphi_{\lambda_{k+1}}$ is not “too different” from φ_{λ_k} , in the sense that we do not want $\mathcal{A}_*^{(k)}$ to jump to a wildly different, possibly malign, local minimum when producing $\mathcal{A}_*^{(k+1)}$.

In our benchmarking experiments described in the main text, the varying noise level prohibits us from carefully tuning λ_{end} , but even without graduated continuation (single refinement, $\lambda_1 = \lambda_0 = 0.5$), the SBD-STM procedure produces qualitatively similar and informative estimates of \mathcal{A}_0 , albeit slightly suboptimal.

IV. APPLICATION TO IMAGE DEBLURRING

In this section, we present an extension of our algorithmic approach that addresses an image deblurring problem in computer vision. Image deblurring aims to recover a sharp natural image from its blurred observation due to some unknown photographic process, such as a shaking camera or defocusing [28–30]. Although natural images are generally not sparse, it is widely acknowledged that sparsity exists in its spatial gradient [28, 31].

Suppose $\mathbf{Y} = \mathbf{A}_0 * \mathbf{X}_0$ is the observed blurry image, which is represented as the convolution of the original sharp image \mathbf{X}_0 and a kernel \mathbf{A}_0 that models the blurring. Owing to the linearity of the convolution operator, the gradient of the observed blurred image must equal the convolution of the blurring kernel \mathbf{A}_0 and the gradient of the original sharp image, which possesses the requisite sparsity needed in our algorithm. For instance, we have in two dimensions:

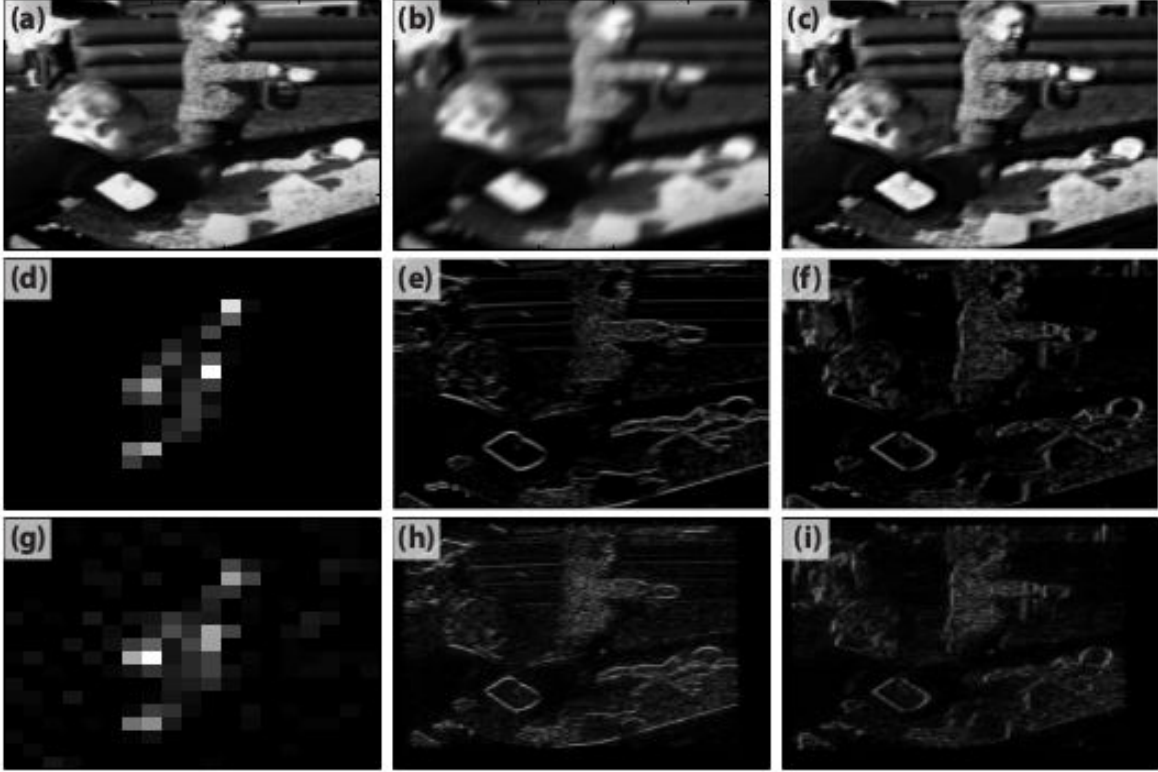
$$\begin{aligned}\nabla_x \mathbf{Y} &= \mathbf{A}_0 * \nabla_x \mathbf{X}_0 \\ \nabla_y \mathbf{Y} &= \mathbf{A}_0 * \nabla_y \mathbf{X}_0\end{aligned}$$

where ∇_x and ∇_y denote derivatives in the x and y directions, respectively. Since the gradients $\nabla_x \mathbf{X}_0$ and $\nabla_y \mathbf{X}_0$ are sparse signals by hypothesis, the image deblurring SBD problem can be cast as the following optimization problem:

$$\min_{\mathbf{A} \in \mathbb{S}_*, \mathbf{X}_x, \mathbf{X}_y} \left[\frac{1}{2} \|\nabla_x \mathbf{Y} - \mathbf{A} * \mathbf{X}_x\|_F^2 + \lambda \cdot r(\mathbf{X}_x) + \frac{1}{2} \|\nabla_y \mathbf{Y} - \mathbf{A} * \mathbf{X}_y\|_F^2 + \lambda \cdot r(\mathbf{X}_y) \right] \quad (\text{S26})$$

where \mathbb{S}_* denotes the intersection of the unit sphere and the positive orthant. The optimization variables \mathbf{X}_x and \mathbf{X}_y correspond to the horizontal and vertical gradients of \mathbf{X} , respectively.

The non-negativity of the blurring kernel \mathbf{A} removes sign ambiguity during the recovery process, contrasted to the STM problem described in Section III A. With minor modifications, the two-stage procedure used for SBD-STM can be applied to image deblurring to determine reliable estimates of the original sharp image. See Supplementary Figure S-V for a demonstration of the image deblurring process using this approach.



Supplementary Figure S-V. Demonstration of image deblurring by solving the SBD problem in (S26). (a) Original sharp image \mathbf{X}_0 (b) Observed blurred image \mathbf{Y} (c) Recovered deblurred image $\hat{\mathbf{X}}$ (d) Ground truth of blurring kernel \mathbf{A}_0 (e) Horizontal gradient of original image $\nabla_x \mathbf{X}_0$ (f) Vertical gradient of original image $\nabla_y \mathbf{X}_0$ (g) Recovered blurring kernel $\hat{\mathbf{A}}$ (h) Recovered horizontal gradient $\hat{\mathbf{X}}_x = \nabla_x \hat{\mathbf{X}}$ (i) Recovered vertical gradient $\hat{\mathbf{X}}_y = \nabla_y \hat{\mathbf{X}}$.

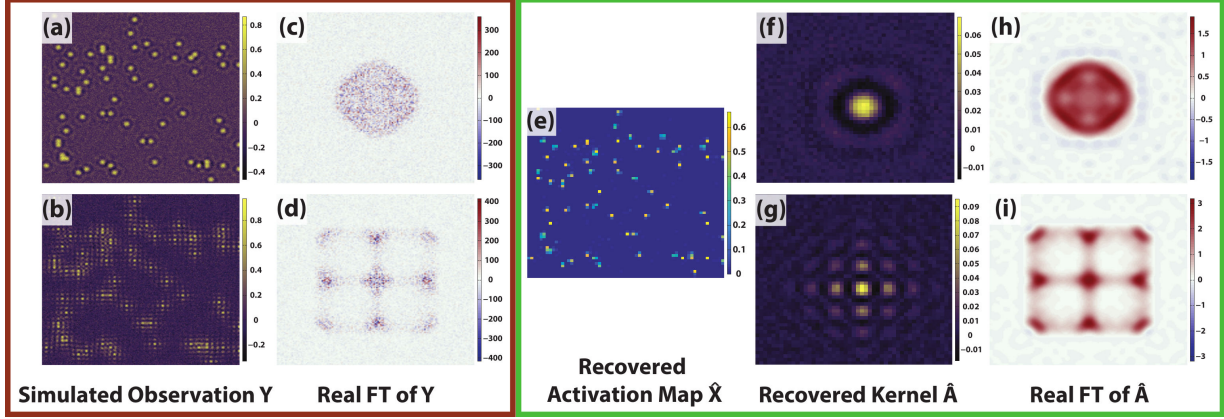
V. SBD-STM ON HIGH-DIMENSIONAL SIMULATED MEASUREMENTS

Using the methods described in Section I, we constructed artificial STM measurements of a material with 70 identical point defects distributed across a 50×50 atomic square lattice. As discussed in the main text, the convolutional data model for STM measurements has the general form:

$$\mathcal{Y} = \mathcal{A} \boxtimes \mathcal{X} + \mathcal{Z}$$

The simulated dataset consisted of 41 constant-bias scans of the same 256×256 pixel measurement grid and included additive zero-mean Gaussian noise. Supplementary Figure S-VI displays the algorithm outputs on two separate slices of simulated data.

The Re-FTs of the raw observations \mathcal{Y} show some faint structure, which is obscured by phase noise associated with random defect locations. By using SBD-STM, one deconvolves the noisy measurement \mathcal{Y} to recover the underlying kernel $\hat{\mathcal{A}}$ and the activation map $\hat{\mathcal{X}}$



Supplementary Figure S-VI. SBD-STM results on simulated noisy STM data with 70 localized defects. Results for the FT-STM and SBD-STM methodologies on the same dataset are enclosed in the red and green boxes, respectively. (a)-(b) Two separate constant-bias slices from the same $\mathcal{Y} \in \mathbb{R}^{256 \times 256 \times 41}$ dataset (c)-(d) The corresponding Re-FT of the simulated observations in (a)-(b), respectively. Shown in the green box are SBD-STM results: (e) the recovered activation map $\hat{\mathcal{X}}$ (globally refined across all 41 bias slices) and (f)-(g) the recovered kernel $\hat{\mathcal{A}}$ for each constant-bias slice of the observed \mathcal{Y} from (a)-(b). (h)-(i) The corresponding Re-FTs of each recovered kernel $\hat{\mathcal{A}}$. There is significant improvement in data fidelity in the SBD-STM results in (h)-(i) compared to results from the standard FT-STM methodology in (c)-(d). All Re-FT spectra are shown with $-3\pi/5a \leq k_x, k_y \leq 3\pi/5a$.

marking the locations of the defects. As shown on the rightmost column of Supplementary Figure S-VI the corresponding FTs of the recovered $\hat{\mathcal{A}}$ are uncontaminated by the phase noise inherent in the FT of \mathcal{Y} , leaving behind the “true” structure of the defect. The strong peaks Re-FT spectrum present in these images are consistent with the allowed elastic scatterings of the underlying square lattice. Such observations are less evident from Re-FTs of the original \mathcal{Y} since phase noise suppresses the strong peaks.

VI. BENCHMARKING THE SBD-STM APPROACH

We use the artificial STM data in the previous section to generate measurements \mathcal{Y} for assessing the SBD-STM’s ability to provide robust estimates of \mathcal{A}_0 and \mathcal{X}_0 as various measurement parameters are varied. Parameters of interest include the measurement size $n \equiv n_1 \times n_2$, kernel size $m \equiv m_1 \times m_2$, kernel concentration θ , and additive noise variance η . To demonstrate the broad applicability of SBD-STM to multiple modalities of microscopy, we restrict our initial benchmarking datasets to single-energy measurements $\mathcal{Y}_{\theta,\eta} \in \mathbb{R}^{n_1 \times n_2}$.

Under the convolutional data model, each observation is generated through the process:

$$\mathcal{Y}_{\theta,\eta} = \tilde{\mathcal{A}}_0 \boxtimes \mathcal{X}_\theta + \mathcal{Z}_\eta \quad (\text{S27})$$

where $\tilde{\mathcal{A}}_0 \in \mathbb{R}^{n_1 \times n_2}$ is the zero-padded extension of the truth kernel $\mathcal{A}_0 \in \mathbb{R}^{m_1 \times m_2}$, which is chosen from TB simulation results described in Section I. The stochastic contributions for each measurement $\mathcal{Y}_{\theta,\eta}$ are contained in the random activation map $\mathcal{X}_\theta \in \mathbb{R}^{m_1 \times m_2}$ as a Bernoulli process with parameter θ and in $\mathcal{Z}_\eta \in \mathbb{R}^{m_1 \times m_2}$ as zero-mean Gaussian noise process with variance η .

A series of independent measurements is produced following (S27) for several candidate values of θ and η . Each artificial measurement $\mathcal{Y}_{\theta,\eta}$ is processed by SBD-STM, yielding estimates $\hat{\mathcal{A}}_{\theta,\eta}$ and $\hat{\mathcal{X}}_{\theta,\eta}$ of $\hat{\mathcal{A}}_0$ and $\hat{\mathcal{X}}_\theta$, respectively. To reduce experimental ambiguity, the SBD-STM regularizer parameter λ is fixed at 0.5 for these benchmarking trials. In practice, λ can be appropriately adjusted to suit specific measurement and model parameters, leading to results that are generally favorable to SBD-STM outputs with fixed λ . As described in the main text, we assess the quality of SBD-STM kernel recovery by defining the real-space error metric:

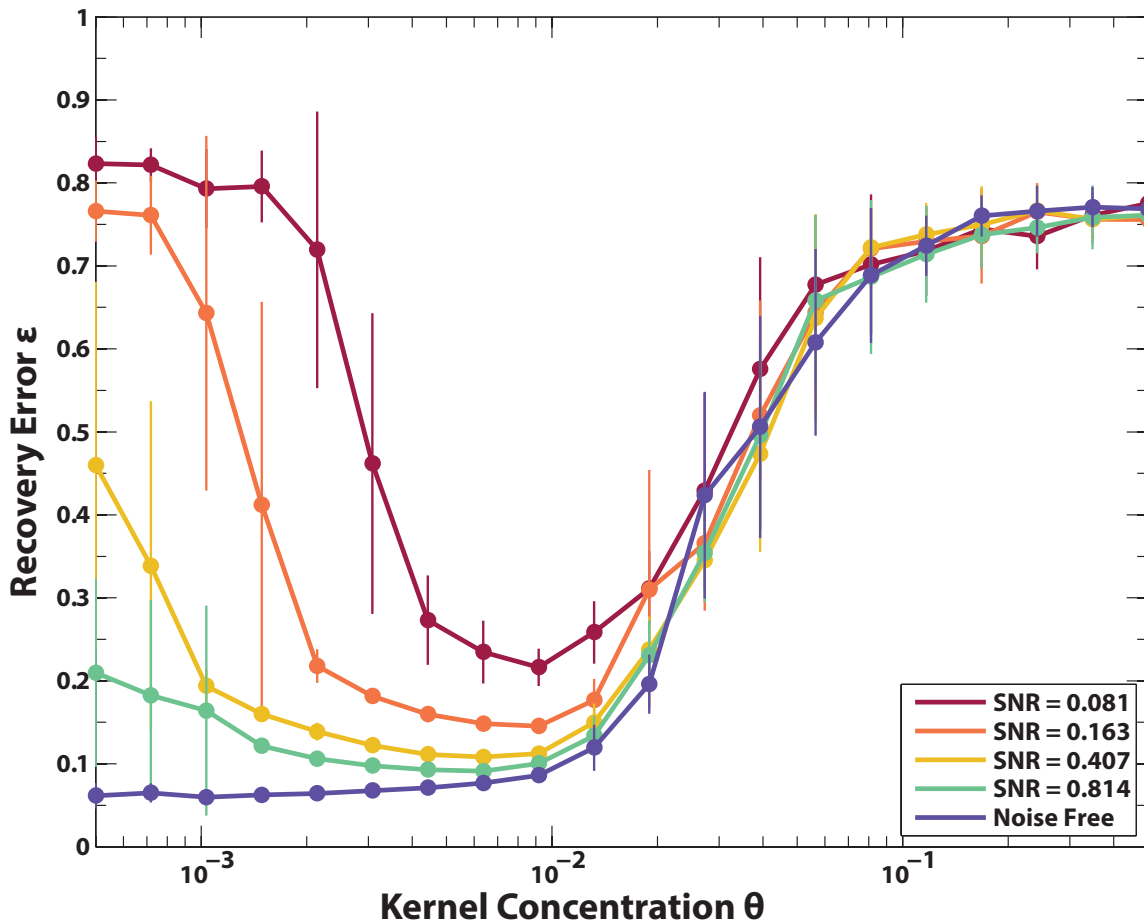
$$\epsilon(\hat{\mathcal{A}}_{\theta,\eta}, \mathcal{A}_0) \equiv \frac{2}{\pi} \arccos \left| \langle \hat{\mathcal{A}}_{\theta,\eta}, \mathcal{A}_0 \rangle \right|$$

where $\langle \hat{\mathcal{A}}_{\theta,\eta}, \mathcal{A}_0 \rangle \in [-1, 1]$ denotes the inner product between vectorizations of $\hat{\mathcal{A}}_{\theta,\eta}$ and \mathcal{A}_0 . The mean of $\epsilon(\hat{\mathcal{A}}_{\theta,\eta}, \mathcal{A}_0)$ is the average angle (normalized by $\frac{\pi}{2}$) between the two vectors on the hemisphere. Thus this metric provides an indication of the overall SBD-STM recovery performance for measurements with fixed θ and η while the spread of $\epsilon(\hat{\mathcal{A}}_{\theta,\eta}, \mathcal{A}_0)$ reveals the stability of SBD-STM to stochastic fluctuations ascribed to θ and η .

A. Real Space Error vs Kernel Concentration and High-Amplitude Noise

To explore the evolution of $\epsilon(\hat{\mathcal{A}}_{\theta,\eta}, \mathcal{A}_0)$ on the kernel concentration and a wider range of additive noise variances than in the main text, additional collections of measurements $\mathcal{Y}_{\theta,\eta}$ of fixed size $n = 185 \times 185$ were constructed from (S27) with \mathcal{A}_0 of fixed size $m = 35 \times 35$. 20 independent measurements were made for each ordered pair (θ, η) , with η ranging from 0 to 0.01 and using the same θ values in Figure 4(b) of the main text. A summary of the real-space recovery errors for these trials is shown in Supplementary Figure S-VII. Supplementary

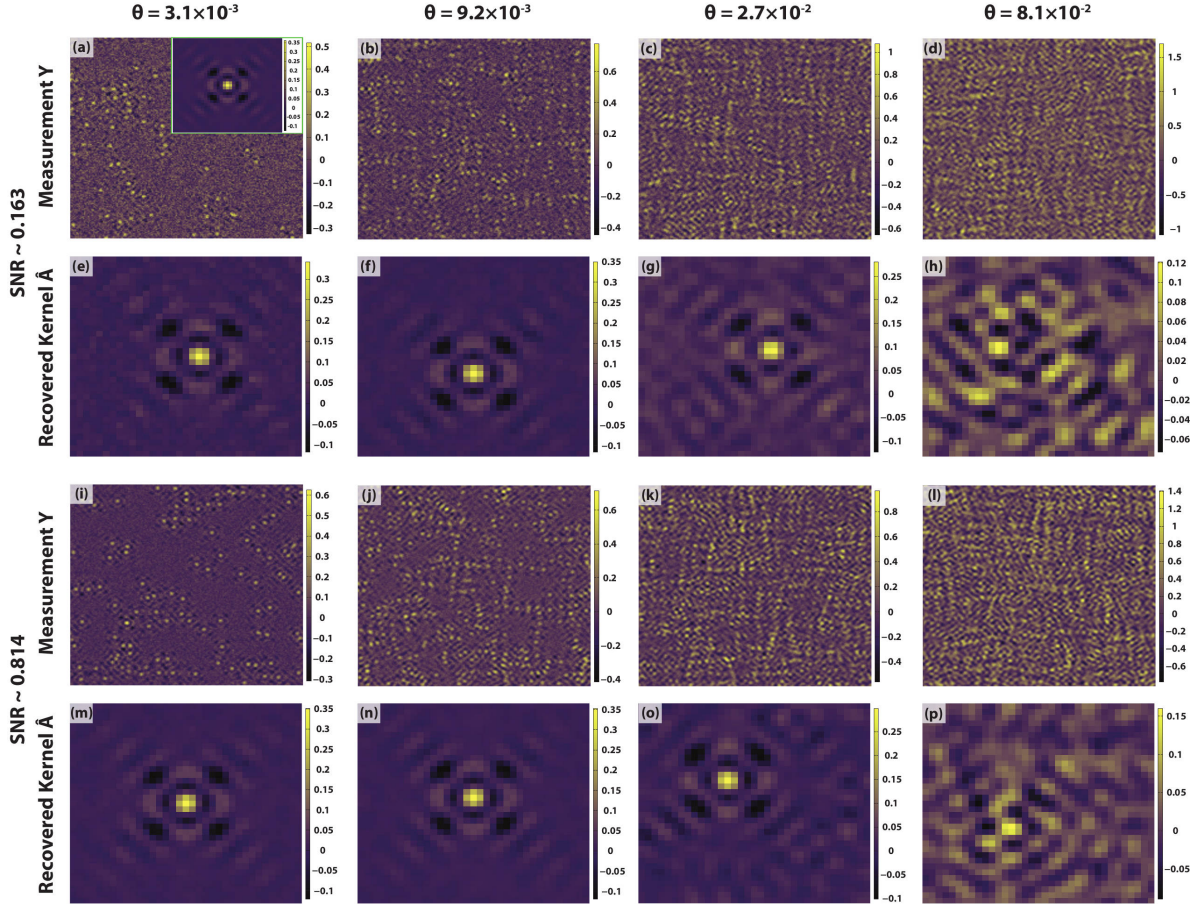
Figure S-VIII shows representative observations $\mathcal{Y}_{\theta,\eta}$ and the corresponding recovered kernel $\hat{\mathcal{A}}_{\theta,\eta}$ for selected SNR and θ values in Supplementary Figure S-VII.



Supplementary Figure S-VII. Averaged real-space errors of the recovered kernel $\hat{\mathcal{A}}_{\theta,\eta} \in \mathbb{R}^{35 \times 35}$ against the truth kernel $\mathcal{A}_0 \in \mathbb{R}^{35 \times 35}$ in 20 independent simulated STM measurements $\mathcal{Y}_{\theta,\eta} \in \mathbb{R}^{185 \times 185}$. Solid lines indicate the kernel recovery error $\epsilon(\hat{\mathcal{A}}_{\theta,\eta}, \mathcal{A}_0)$ vs. kernel concentration θ in the presence of additive Gaussian noise with variance η . Examples of simulated measurements in this figure and their corresponding SBD-STM recovered kernels are shown in Supplementary Figure S-VIII.

B. Fourier Space Error Comparison

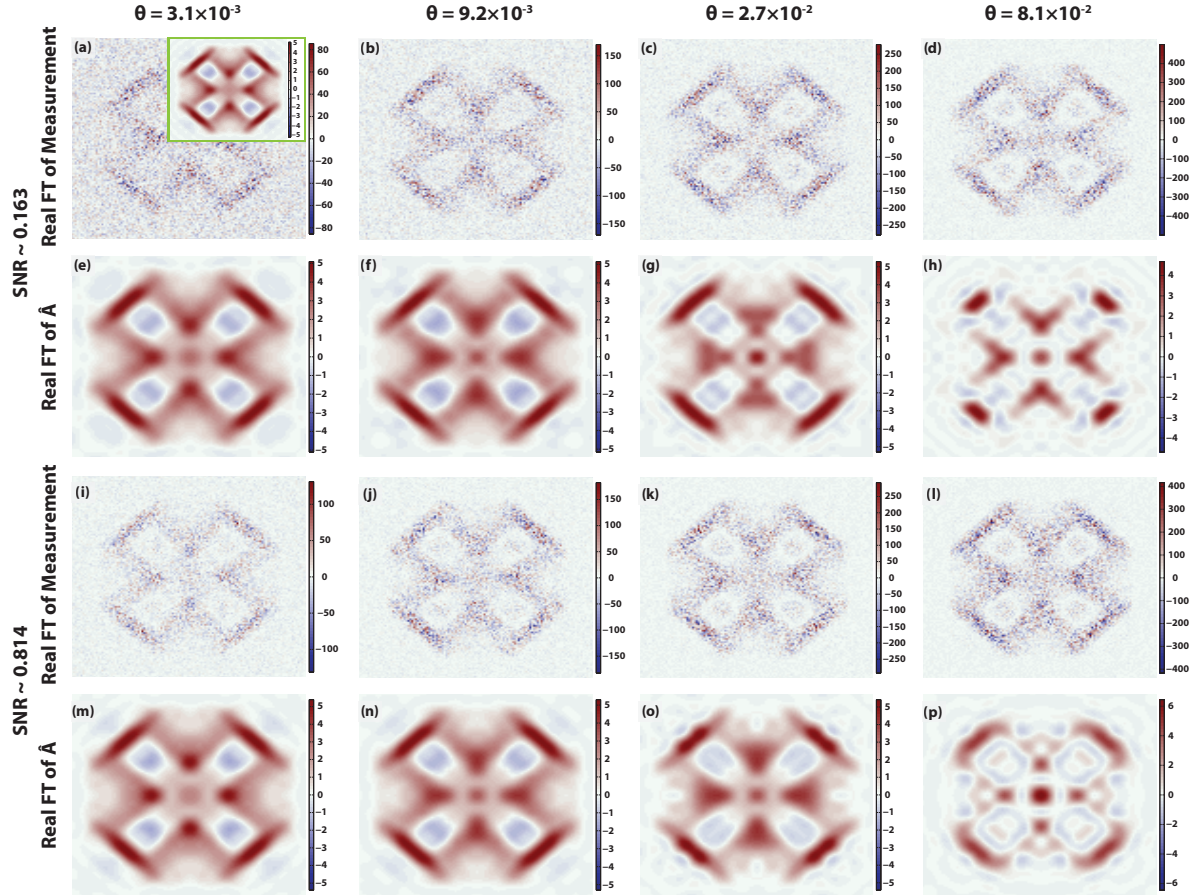
Supplementary Figure S-IX displays the Real Part of the FTs (Re-FTs) of the real-space results presented in Supplementary Figure S-VIII. From these examples, one observes that the Fourier-space errors from raw measurements $\mathcal{Y}_{\theta,\eta}$ gradually improve with increasing concentration. However, the presence of phase noise and experimental noise washes away



Supplementary Figure S-VIII. (a)-(p) Example measurements and recovered kernels for select kernel concentrations and SNRs from Supplementary Figure S-VII. The truth defect pattern \mathcal{A}_0 for these measurements is shown in the inset of (a). SBD-STM is able to recover a reasonable estimate of the defect kernel $\hat{\mathcal{A}}$, even with poor SNR ≈ 0.163 that prohibits reliable deconvolution by inspection. These kernel estimates also include detailed interference patterns surrounding the bright peak in the LDoS, which are visually obscured in \mathcal{Y} by the high noise levels.

the detailed structure found in the FT of the truth kernel. The corresponding Fourier-space errors from $\hat{\mathcal{A}}$ exhibit similar trends as the real-space errors with increasing concentration. There is an improvement in the FT errors as the kernel concentration is increased to a range spanning $0.001 \lesssim \theta \lesssim 0.01$. However, even in the high concentration limit (right-most column) the Re-FT of $\hat{\mathcal{A}}$ possesses many detailed features present in the truth kernel Re-FT that are absent in the Re-FT of $\mathcal{Y}_{\theta,\eta}$.

[1] Neil W. Ashcroft and Nathaniel David Mermin, *Solid State Physics* (Cengage Learning, 1976).



Supplementary Figure S-IX. (a)-(p) Re-FTs of the raw observations and recovered kernels from Supplementary Figure S-VIII. All Re-FT spectra are shown with $-3\pi/5a \leq k_x, k_y \leq 3\pi/5a$. The Re-FT of the truth defect pattern \mathcal{A}_0 for these results is shown in the inset of (a). Phase-sensitive recovery of the scattering patterns is only observed in the Re-FT of recovered kernels. Note the difference in the colorbar scales between the Re-FT of the original measurements and recovered kernels.

- [2] Michael Marder, *Condensed Matter Physics*, 2nd ed. (Wiley, 2010).
- [3] E.N. Economou, *Green's Functions in Quantum Physics*, 3rd ed., Springer Series in Solid-State Sciences (Springer, 2006).
- [4] C.J. Chen, *Introduction to Scanning Tunneling Microscopy*, Monographs on the Physics and Chemistry of Materials (Oxford University Press, 2008).
- [5] David L Donoho and Michael Elad, "Optimally sparse representation in general (nonorthogonal) dictionaries via l1 minimization," *Proceedings of the National Academy of Sciences* **100**, 2197–2202 (2003).
- [6] Emmanuel J Candes and Terence Tao, "Decoding by linear programming," *IEEE transactions on information theory* **51**, 4203–4215 (2005).

- [7] Roman Vershynin, “Introduction to the non-asymptotic analysis of random matrices,” arXiv preprint arXiv:1011.3027 (2010).
- [8] Trevor Hastie, Robert Tibshirani, and Martin Wainwright, *Statistical learning with sparsity: the lasso and generalizations* (CRC Press, 2015).
- [9] Martin J Wainwright, “Sharp thresholds for high-dimensional and noisy sparsity recovery using-constrained quadratic programming (lasso),” *IEEE transactions on information theory* **55**, 2183–2202 (2009).
- [10] Emmanuel J Candes and Terence Tao, “Near-optimal signal recovery from random projections: Universal encoding strategies?” *IEEE transactions on information theory* **52**, 5406–5425 (2006).
- [11] Emmanuel Candes and Justin Romberg, “Sparsity and incoherence in compressive sampling,” *Inverse problems* **23**, 969 (2007).
- [12] Simon Foucart and Holger Rauhut, *A mathematical introduction to compressive sensing*, Vol. 1 (Springer, 2013).
- [13] Michael Lustig, David L Donoho, Juan M Santos, and John M Pauly, “Compressed sensing mri,” *IEEE Signal Processing Magazine* **25**, 72–82 (2008).
- [14] Alan V Oppenheim and Ronald W Schaffer, *Discrete-time signal processing* (Pearson Higher Education, 2010).
- [15] Ali Ahmed, Benjamin Recht, and Justin Romberg, “Blind deconvolution using convex programming,” *IEEE Transactions on Information Theory* **60**, 1711–1732 (2014).
- [16] Yanjun Li, Kiryung Lee, and Yoram Bresler, “Identifiability in blind deconvolution with subspace or sparsity constraints,” *IEEE Transactions on Information Theory* **62**, 4266–4275 (2016).
- [17] Yuejie Chi, “Guaranteed blind sparse spikes deconvolution via lifting and convex optimization,” *IEEE Journal of Selected Topics in Signal Processing* **10**, 782–794 (2016).
- [18] Emmanuel J Candès and Carlos Fernandez-Granda, “Towards a mathematical theory of super-resolution,” *Communications on Pure and Applied Mathematics* **67**, 906–956 (2014).
- [19] Eftychios A Pnevmatikakis, Daniel Soudry, Yuanjun Gao, Timothy A Machado, Josh Merel, David Pfau, Thomas Reardon, Yu Mu, Clay Lacefield, Weijian Yang, *et al.*, “Simultaneous denoising, deconvolution, and demixing of calcium imaging data,” *Neuron* **89**, 285–299 (2016).

- [20] Anat Levin, Yair Weiss, Fredo Durand, and William T Freeman, “Understanding and evaluating blind deconvolution algorithms,” in *2009 IEEE Conference on Computer Vision and Pattern Recognition* (2009) pp. 1964–1971.
- [21] Subhasis Chaudhuri, Rajbabu Velmurugan, and Renu Rameshan, *Blind Image Deconvolution: Methods and Convergence*, 1st ed. (Springer International Publishing, 2014).
- [22] Patrizio Campisi and Karen Egiazarian, *Blind image deconvolution: theory and applications* (CRC press, 2016).
- [23] P-A Absil, Robert Mahony, and Rodolphe Sepulchre, *Optimization algorithms on matrix manifolds* (Princeton University Press, 2009).
- [24] Jason D Lee, Max Simchowitz, Michael I Jordan, and Benjamin Recht, “Gradient descent converges to minimizers,” University of California, Berkeley **1050**, 16 (2016).
- [25] Rong Ge, Furong Huang, Chi Jin, and Yang Yuan, “Escaping from saddle pointsonline stochastic gradient for tensor decomposition,” in *Proceedings of The 28th Conference on Learning Theory* (2015) pp. 797–842.
- [26] N. Boumal, B. Mishra, P.-A. Absil, and R. Sepulchre, “Manopt, a Matlab toolbox for optimization on manifolds,” *Journal of Machine Learning Research* **15**, 1455–1459 (2014).
- [27] Kimon Fountoulakis and Jacek Gondzio, “A second-order method for strongly convex ℓ_1 -regularization problems,” *Mathematical Programming* **156**, 189–219 (2016).
- [28] A. Levin, Y. Weiss, F. Durand, and W. Freeman, “Understanding blind deconvolution algorithms,” *IEEE Transactions on Pattern Analysis and Machine Intelligence* **33**, 2354–2367 (2011).
- [29] D. Kundur and D. Hatzinakos, “Blind image deconvolution,” *Signal Processing Magazine, IEEE* **13**, 43–64 (1996).
- [30] Dilip Krishnan and Rob Fergus, “Fast image deconvolution using hyper-laplacian priors,” in *Advances in Neural Information Processing Systems 22*, edited by Y. Bengio, D. Schuurmans, J. D. Lafferty, C. K. I. Williams, and A. Culotta (Curran Associates, Inc., 2009) pp. 1033–1041.
- [31] Rob Fergus, Barun Singh, Aaron Hertzmann, Sam T. Roweis, and William T. Freeman, “Removing camera shake from a single photograph,” *ACM Trans. Graph.* **25**, 787–794 (2006).